Supplementary Information

Engineered interfaces in indium-hafnium oxide catalysts unlock superior methanol productivity

*Yung-Tai Chiang,[a,b] Milica Ritopecki,[c,d] Patrik O. Willi,[a,b] Katja Raue,[b,e] Jordi Morales-Vidal,[c] Tangsheng Zou,[a,b] Mikhail Agrachev,[b,e] Henrik Eliasson,[f] Jianyang Wang,[a,b] Rolf Erni,[f] Wendelin J. Stark,[a,b] Gunnar Jeschke,[b,e] Robert N. Grass,[a,b] Núria López,[c] Sharon Mitchell,[a,b] and Javier Pérez-Ramírez[a,b]**

[a] Institute for Chemical and Bioengineering, Department of Chemistry and Applied Biosciences, ETH Zurich, Vladimir-Prelog-Weg 1, 8093 Zurich, Switzerland.

[b] NCCR Catalysis, Zurich, Switzerland.

[c] Institute of Chemical Research of Catalonia (ICIQ-CERCA), The Barcelona Institute of Science and Technology, Av. Països Catalans 16, 43007 Tarragona, Spain.

[d] Universitat Rovira i Virgili, Av. Catalunya 35, Tarragona 43002, Spain.

[e] Institute of Molecular Physical Science, Department of Chemistry and Applied Biosciences, ETH Zurich, Vladimir-Prelog-Weg 1, 8093 Zurich, Switzerland.

[f] Electron Microscopy Center, Empa - Swiss Federal Laboratories for Materials Science and Technology, Uberlandstrasse 129, 8600 Dubendorf, Switzerland.

* Corresponding author: jpr@chem.ethz.ch

Table of Contents

Supplementary Note 1: DFT modelling approach for In-Hf mixed oxides.

Selection of HfO_2 polymorph. At ambient pressure, HfO_2 can adopt three crystalline polymorphs; monoclinic (m), tetragonal (t), and cubic (c), which interconvert with temperature. m-HfO_2 is thermodynamically stable at room temperature and transforms into t-HfO_2 and then to c-HfO_2 upon heating. The monoclinic-to-tetragonal and tetragonal-to-cubic transitions occur at ~2000 K and ~2870 K, respectively, and c-HfO_2 melts at 3031 K. Alternatively, for ZrO_2, The monoclinic-to-tetragonal and tetragonal-to-cubic transitions occur at ~1480 K and ~2650 K, respectively, which are significantly lower than the transition temperature of HfO_2[1].

XRD analysis of bulk phases shows that, depending on the preparation method and In_2O_3 content, indium-hafnium mixed oxide catalysts may contain either only m-HfO_2, or a mixture of monoclinic, tetragonal, and cubic polymorphs. Surface-sensitive Raman spectroscopy indicates mainly m-HfO_2, except at high In_2O_3 content, where features shift toward c-HfO_2. Considering that the best-performing catalysts exhibited predominantly or exclusively the monoclinic polymorph, we focused on this phase. However, we also simulated structures based on t/c-HfO_2 for comparison.

Substitution of indium single atoms in the bulk of HfO_2. The crystal symmetry and coordination of HfO_2 polymorphs are characterized as follows:

m-HfO_2 $(P2_1/c)$: $a \neq b \neq c$; $\alpha = \gamma = 90^o \neq \beta$. Hf atoms are 7-fold coordinated, whereas O can have 3- or 4-fold coordination.

t-HfO_2 $(P4_2/nmc)$: $a = b \neq c$; $\alpha = \beta = \gamma = 90^o$. Two distinct Hf−O bond lengths. Hf atoms are 8-fold coordinated, and O atoms are 4-fold coordinated.

c-HfO_2 $(Fm\bar{3}m)$: $a = b = c$; $\alpha = \beta = \gamma = 90^o$. Hf−O bond distances are equivalent throughout, with the same coordination as t-HfO_2.

Supercells (2×2×2 for monoclinic and cubic, 2×2×3 for tetragonal) were constructed to match experimental indium contents for 2 wt% In_2O_3, which showed the best performance.

Since each polymorph contains only a single type of metal cation, lattice substitution of indium was examined by replacing a Hf atom with an In atom (**Supplementary Fig. 6**) and was found to be energetically favourable in the monoclinic lattice.

Oxygen vacancy formation was studied for the pristine and In-containing bulk models. For m-HfO_2, vacancies were introduced at both 3-fold and 4-fold coordinated O sites, whereas only one symmetry unique O site exists in t-HfO_2 and c-HfO_2. For In-containing systems, all non-equivalent O atoms in the first coordination sphere were assessed (seven for m-HfO_2, two for t-HfO_2, and one for c-HfO_2. The results (**Supplementary Fig. 6**) show that the presence of oxygen vacancies makes the stabilization of lattice-substituted indium atoms more favourable within the bulk, particularly in the cubic polymorph, and that oxygen vacancy formation is favoured when indium atoms are present.

Analysis of In speciation. AC-STEM images confirm the atomic dispersion of InO_x species, likely as indium single atoms. Since isolated indium sites have rarely been explored within the active ensembles of In_2O_3-based catalysts for CO_2 hydrogenation, density functional theory (DFT) simulations were performed on indium species adsorbed to the surface of the HfO_2 support in ligand-free or oxyhydroxylated form. The formation of neighbouring oxygen vacancies was also studied in each case. Thermodynamics of reaction paths were calculated for CO_2 hydrogenation to methanol and the competing reverse water-gas shift (RWGS) reaction.

Stabilization of isolated In sites at the surface and subsurface of HfO_2. To evaluate the stabilization of In single atoms by HfO_2, we constructed slab models by cleaving the optimized bulk lattices of the monoclinic and tetragonal phases (**Supplementary Fig. 11**). The most stable oxygen-terminated surfaces were selected: (–111) for m-HfO_2 and (101) for t-HfO_2, respectively. The slabs were constructed with $p(1\times1)$ and $p(1\times2)$ surface unit cells, respectively, with an identical number of layers, formula units, and ratio of relaxed-to-fixed atoms[2].

Three types of In single-atom species were assessed. Substitution models involved replacing a surface or subsurface Hf atom with an In atom. Adsorption models considered the

deposition of an isolated In atom on top of the surface oxygen atoms. Finally, hydroxylated adsorption models involved the deposition of $In(OH)_3$ species on the same surface, in which case surface unit cells twice the size of those mentioned were used to prevent the interaction between adsorbed species.

Each configuration was studied in the presence and absence of a neighbouring oxygen vacancy. In the substitution model for m-HfO_2 (–111), the slab contains eight non-equivalent Hf sites: five bulk-like 7-fold coordination (four subsurface, one surface) and three 6-fold-coordinated surface atoms (**Supplementary Fig. 12**). In t-MO_2 (101), the slab contains four Hf atoms in each of the surface and subsurface layers; the surface Hf atoms are 7-fold coordinated, while the subsurface atoms are 8-fold coordinated, as in the bulk. Non-equivalency arises from distinct M−O bond lengths. Substitution of In atoms is generally more favourable at surface and subsurface sites than in the bulk of the support (**Supplementary Fig. 14**), and lower incorporation energies are observed for the monoclinic than the tetragonal phase. The adsorption of isolated In atoms is endothermic, leading to physisorption. In contrast, the adsorption of $In(OH)_3$ adatoms is consistently exothermic, with oxygen atoms acting as anchoring sites on both monoclinic and tetragonal HfO_2 surfaces (**Supplementary Fig. 18**).

Oxygen vacancy formation was examined for pristine (m-/t-)HfO_2 slabs, for lattice-substituted In single atoms, and for adsorbed $In(OH)_3$ species, which are detailed in **Supplementary Figs. 13**, **15**, and **19**, respectively. For the pristine systems, vacancy formation was simulated at all non-equivalent oxygens. In m-HfO_2(–111), 16 non-equivalent oxygen sites were identified (8 subsurface, 8 surface), mainly 3- or 4-fold coordinated, with one 2-fold coordinated surface site. In t-MO_2(101), eight non-equivalent oxygens were found (four subsurface, four surface), with each layer containing two 3-fold and two 4-fold (bulk-like) coordinated oxygens. Substituting a single Hf atom with In (**Supplementary Fig. 12**) and testing each non-equivalent O site revealed that oxygen vacancies stabilize surface In incorporation, particularly in the tetragonal polymorph (**Supplementary Fig. 15**). In addition

to the lattice O sites, in $In(OH)_3$-HfO_2 systems, three potential vacant sites from hydroxyl groups were examined. The most favourable oxygen vacancy is located directly above (on top) the adsorbed In atom (**Fig. 3, Supplementary Fig. 19**).

Energetics and stability of the $InHfO_x$ models. The relative stability of pristine m-, t-, and c-HfO_2 polymorphs was evaluated by calculating their formation energies (E_f), as defined in **Supplementary Equations 1** and **2**. Reference energies were taken from DFT simulations by formula unit of each HfO_2 polymorph ($E^{DFT}_{HfO_2,bulk}$), bulk hafnium ($E^{DFT}_{Hf,bulk}$), and molecular oxygen ($E^{DFT}_{O_2,gas}$):

$$Hf + O_2 \longrightarrow HfO_2 \quad (1)$$

$$E_f = E^{DFT}_{HfO_2,\,bulk} - E^{DFT}_{Hf,\,bulk} - E^{DFT}_{O_2,\,bulk} \quad (2)$$

The potential energy (E) of the bulk and slab HfO_2 systems was then determined (**Supplementary Equations 3** and **4**) to assess the relative stability of models with oxygen vacancies and or incorporated In atoms. The reference energies for these calculations were molecular H_2 ($E^{DFT}_{H_2,gas}$), H_2O ($E^{DFT}_{H_2O,gas}$), bulk In metal ($E^{DFT}_{In,bulk}$), and prisitine bulk supercell or slab (Hf_xO_y) of each polymorph. Here, v denotes the number of oxygen vacancies and s the number of incorporated In atoms:

$$Hf_xO_y + sIn + (-2s+v) + H_2 \longrightarrow In_sHf_{x-s}Hf_{y-v} + sHfO_{2,bulk}(-2s+v) + H_2O \quad (3)$$

$$E = E^{DFT}_{In_sHf_{x-s}O_{y-v}} + sE^{DFT}_{HfO_2,bulk} + (-2s+v)E^{DFT}_{H_2O,gas} - sE^{DFT}_{Hf,bulk} - sE^{DFT}_{O_2,bulk} - (-2s+v)E^{DFT}_{H_2,gas} \quad (4)$$

The oxygen vacancy formation energy (E_{vac}) was obtained using **Supplementary Equation 5** to identify the most stable vacancy site and assess the likelihood of vacancy formation:

$$E_{vac} = E^{DFT}_{In_sM_{x-s}O_{y-v+1}} + E^{DFT}_{H_2O,gas} - E^{DFT}_{In_sM_{x-s}O_{y-v}} - E^{DFT}_{H_2,gas} \quad (5)$$

The segregation energy (E_{seg}) of each polymorph was calculated to quantify the tendency of In atoms to migrate from bulk to subsurface or surface sites (**Supplementary Equation 6**):

$$E_{seg} = E_{In@subsurface/surface} + E_{In@bulk} \quad (6)$$

Finally, the aggregation energy indicates the tendency of $In(OH)_3$ species to form dimers on the surface (**Supplementary Equation 7**):

$$E_{agg} = 2E_{In(OH)_3@surface} - E_{2(In(OH)_3)@surface} - E_{surface} \quad (7)$$

Simulation of In-Zr mixed oxides. Since atomically dispersed In atoms have not previously been modelled as active sites in CO_2 hydrogenation to methanol, for comparison, an identical set of simulations was conducted for ZrO_2 by replacing Hf with Zr[3,4]. ZrO_2 undergoes the same polymorphic sequence as HfO_2, but the m-t transition occurs at lower temperature (~1480 K) and the t-c transition at ~2650 K. XRD analyses indicate the bulk crystalline phase consists either of m-ZrO_2, or a mixture of m- and t-ZrO_2. A small fraction of t-ZrO_2 is also detectable at the surface, but it decreases during CO_2 hydrogenation.

Supplementary Note 2: Electronic structure and oxygen vacancy dynamics.

Oxygen vacancy density is a key descriptor in In_2O_3-based catalysts for CO_2 hydrogenation to methanol[5,6], and depends on the synthesis methods and history of thermal or chemical treatments of the catalyst. For binary catalytic systems prepared by flame spray pyrolysis, formation of intrinsic defects is favoured owing to the rapid quenching rate and presence of heterovalent dopants. Fundamentally, oxygen vacancy generation is associated with the removal of (sub)surface lattice oxygen, releasing two electrons that may be trapped at the vacancy site and adjacent M^{4+} ion (M = Hf, Zr). This process traps a single electron in the oxygen vacancy ($V_O^{\bullet}$, $g_{iso} = 2.004$) and forms an M^{3+} ion ($g_{xx} = g_{yy} = 1.98$, $g_{zz} = 1.96$). While both signals are observed in the EPR profile of fresh $2InZrO_x$, only the former is recorded in fresh $2InHfO_x$ catalyst (**Fig. 5b**, **Supplementary Figs. 30-31**). This difference points to distinct electronic structures of the vacancy and neighbouring M^{4+} ion. Formation of the $V_O^{\bullet}$-M^{3+}

structure is thermodynamically preferred in m-ZrO_2, whereas the vacancy with two electrons ($V_O^{\bullet\bullet}$-M^{4+}) is more stable in m-HfO_2. Still, the presence of a $V_O^{\bullet}$ signal in 2InHfO_x indicates that some electrons are trapped at isolated defective sites. Under controlled operating conditions (He, H_2, CO_2, and CO_2+H_2), the $V_O^{\bullet}$ signal in 2InHfO_x remains virtually unchanged, indicating that it is likely a spectator species. In contrast, $V_O^{\bullet\bullet}$ is likely the more relevant fingerprint for active sites, though it remains silent in electron paramagnetic resonance (EPR) since the vacancy contains paired electrons.

For 2InZrO_x, thermal treatment in He reoxidises Zr^{3+} to Zr^{4+}, attributed to the transfer of trapped electrons from M sites to thermally-induced oxygen vacancies[5,6]. Exposure to CO_2 heals the isolated oxygen vacancies, leaving only stable superoxides (O^{2-}, $g_{zz} = 2.035$, $g_{yy} = 2.01$, $g_{xx} = 2.002$) on the surface. Upon H_2 treatment, additional vacant sites form via reduction, and the released lattice oxygens combine with surface electrons to yield superoxide species. Finally, introducing the reaction mixture (CO_2 + H_2) removes the superoxide signal and increases the oxygen vacancy density, as evidenced by the higher $V_O^{\bullet}$ signal and a more intense ferromagnetic signal (V_O-f, ~5 G) from strongly coupled oxygen vacancies.

Supplementary Note 3: DFT simulation of reaction thermodynamics.

We computed the thermodynamics of reaction paths for CO_2 hydrogenation to methanol via the formate pathway, along with the competitive RWGS path yielding CO (**Fig. 6a, Supplementary Figs. 38-40**). Simulations were performed on m-HfO_2, m-ZrO_2, and t-ZrO_2, as the experimentally observed surfaces. In each case, we considered adsorbed $In(OH)_3$ species with one oxygen vacancy on top of the adsorbed In atom, as the most representative models of the 2InHfO_x and 2InZrO_x catalysts (see **Supplementary Note 1**).

On m-InHfO_x and m-InZrO_x, CO_2 adsorption occurs via carbonate formation; one oxygen atom of CO_2 binds to the adsorbed In atom, while the carbon bonds to an oxygen from a hydroxide ligand. On t-InZrO_x, in contrast, CO_2 binds at a lattice oxygen site adjacent to the

indium atom. H_2 activation proceeds heterolytically, generating an In−H/OH pair on the surface. In the methanol pathway, the hydride from In−H is transferred to the carbon of the adsorbed CO_2 species, producing formate (CHO_2). A second heterolytic H_2 splitting precedes two additional hydrogenation steps: a hydride transfer to the carbon forming CH_2O_2, followed by proton transfer to the oxygen, yielding formic acid (CH_2OOH). Dehydration of CH_2OOH produces CH_2O and H_2O. A third heterolytic H_2 activation and hydride/proton transfers lead to methoxy (CH_3O) formation and finally methanol. In the RWGS route, the initial intermediate is carboxylate (COOH) rather than formate. Its dehydration yields CO and H_2O.

Supplementary Note 4: Kinetic modelling and performance predictions.

Notation. A microkinetic model developed previously[6-8] was adapted and fitted to experimental data for CO_2 hydrogenation over the $2InHfO_x$ and $2InZrO_x$ catalysts. Experimental conditions varied across *T*, *P*, *GHSV*, and H_2/CO_2 ratio. Over 100 catalytic tests were conducted to obtain a robust dataset for kinetic model fitting. The full experimental data is available through the Zenodo repository (doi:10.5281/zenodo.16881810).

Two reaction pathways were considered consistent with mechanistic insights: Methanol formation from CO_2 (denoted subscript 'MeOH') and CO formation through the reverse water-gas shift reaction (denoted subscript 'RWGS'). Surface reactions were modelled using a two-site Langmuir-Hinshelwood-Hougen-Watson (LHHW) mechanism. The following notations are used:

p_i	partial pressure of compound *i*
r_n	reaction rate of elementary step *n*
k_n, k_{-n}	forward and backward rate coefficients for elementary step *n*
θ_i	surface coverage of compound *i*

$K_i = \frac{k_{\text{ads},i}}{k_{\text{des},i}} = \frac{\theta_i}{p_i}$ adsorption equilibrium for compound *i*

θ_* fraction of free adsorption sites for CO_2, CO, HCOO, CH_3O, CH_3OH

$\theta_\#$ fraction of free adsorption sites for H and H_2O

Rate expressions. In the two-site model, gaseous CO_2, CO, and CH_3OH competitively adsorb on site *, where carbon-containing intermediates such as formate (HCOO), methoxy (CH_3O) also adsorb. Meanwhile H_2O adsorption and dissociative H_2 adsorption occur on site #. The elementary steps considered for MeOH formation are:

(1) k_1, k_{-1} $CO_2* + H^\# \rightleftharpoons HCOO* + \#$

(2) k_2, k_{-2} $HCOO* + H^\# \rightleftharpoons H_2COO* + \#$

(3) k_3, k_{-3} $H_2COO* + H^\# \rightleftharpoons H_2COOH* + \#$

(4) k_4, k_{-4} $H_2COOH* + H^\# \rightleftharpoons CH_2O* + H_2O^\#$

(5) k_5, k_{-5} $CH_2O* + H^\# \rightleftharpoons CH_3O* + \#$

(6) k_6, k_{-6} $CH_3O* + H^\# \rightleftharpoons CH_3OH* + \#$

For CO formation via RWGS, the elementary steps considered are:

(7) k_7, k_{-7} $CO_2* + H^\# \rightleftharpoons COOH* + \#$

(8) k_8, k_{-8} $COOH* + H^\# \rightleftharpoons CO* + H_2O^\#$

The rate-determining steps are assumed as follows: For MeOH formation, the combination of steps (4) and (5) leads to the rate expressions shown in **Equations 8** and **9**:

$$r_{\text{MeOH}} = k_4 k_5 \theta_{\text{H}_2\text{COOH}} \theta_{\text{H}}^2 - k_{-4} k_{-5} \theta_{\text{CH}_3\text{O}} \theta_{\text{H}_2\text{O}} \theta_\# \quad (8)$$

$$= k_{\text{A}} \frac{\theta_\#^2 \theta_*}{\sqrt{p_{\text{H}_2}}} \left(p_{\text{CO}_2} p_{\text{H}_2}^3 - \frac{p_{\text{CH}_3\text{OH}} p_{\text{H}_2\text{O}}}{K_{\text{eq,MeOH}}} \right) \quad (9)$$

where k_A denotes the reaction rate coefficient for methanol formation. For CO formation, step (8) is rate-determining resulting in the rate expressions given in **Equations 10** and **11**:

$$r_{\mathrm{RWGS}} = k_8\theta_{\mathrm{COOH}}\theta_{\mathrm{H}} - k_{-8}\theta_{\mathrm{H_2O}}\theta_{\mathrm{CO}} \tag{10}$$

$$= k_{\mathrm{B}}\theta_{\#}\theta_{*}\left(p_{\mathrm{CO_2}}p_{\mathrm{H_2}} - \frac{p_{\mathrm{H_2O}}p_{\mathrm{CO}}}{K_{\mathrm{eq,RWGS}}} \right) \tag{11}$$

where k_B denotes the reaction rate coefficient for CO formation.

Site balance and free site fraction. In addition to adsorbed CO_2, CO, and CH_3OH, operando DRIFTs experiments (**Fig. 6b,c, Extended Fig. 6, Supplementary Figs. 42-43**) confirmed the presence of formate (HCOO) and methoxy (CH_3O) intermediates, which are included explicitly in the site balance. The free adsorption site fractions on sites * and # are given by the site balance **Equations 12** and **13**:

$$\theta_{*} = \Bigg(1 + K_{\mathrm{CO_2}}p_{\mathrm{CO_2}} + K_{\mathrm{CO}}p_{\mathrm{CO}} + K_{\mathrm{CH_3OH}}p_{\mathrm{CH_3OH}} + K_1K_{\mathrm{CO_2}}p_{\mathrm{CO_2}}\sqrt{K_{\mathrm{H_2}}p_{\mathrm{H_2}}} + \frac{K_6K_{\mathrm{CH_3OH}}p_{\mathrm{CH_3OH}}}{\sqrt{K_{\mathrm{H_2}}p_{\mathrm{H_2}}}} \Bigg)^{-1} \tag{12}$$

$$\theta_{\#} = \frac{1}{1 + \sqrt{K_{\mathrm{H_2}}p_{\mathrm{H_2}}} + K_{\mathrm{H_2O}}p_{\mathrm{H_2O}}} \tag{13}$$

Temperature dependence of rate constants. Overall rate constants for both reactions follow Arrhenius behaviour, referenced to T_{ref} = 573 K, as shown in **Equations 14** and **15**:

$$k_{\mathrm{MeOH}}(T) = k_{\mathrm{MeOH}}\exp\left(\frac{E_{\mathrm{a,MeOH}}}{R}\left(\frac{1}{T_{\mathrm{ref}}} - \frac{1}{T} \right) \right) \tag{14}$$

$$k_{\mathrm{RWGS}}(T) = k_{\mathrm{RWGS}}\exp\left(\frac{E_{\mathrm{a,RWGS}}}{R}\left(\frac{1}{T_{\mathrm{ref}}} - \frac{1}{T} \right) \right) \tag{15}$$

where $E_{a,MeOH}$ and $E_{a,RWGS}$ are the respective activation energies, R = 8.314×10^{-3} kJ mol^{-1} K^{-1}, and k_{MeOH} or k_{RWGS} are the pre-exponential factors. Detailed derivations of these expressions are available in our previous work[6].

Parameter fitting. Predicted molar flows, $F_{i,predicted}$, for species i were calculated by numerically integrating the relevant plug flow reactor (PFR) design equations using the experimental conditions (T, P, and inlet flow rates, $F_{i,inlet}$, derived from the H_2:CO feed ratio and $GHSV$). The fitting minimized the objective function defined in **Equation 16**, representing the normalized sum of squared differences between predicted and experimental outlet molar flows of CH_3OH and CO:

$$\varepsilon = \sum_{n=1}^{n_{total}} \left(\frac{\left(F_{CH_3OH,predicted} - F_{CH_3OH,measured}\right)^2 + \left(F_{CO,predicted} - F_{CO,measured}\right)^2}{F_{CH_3OH,predicted} + F_{CO,predicted}} \right)_n \quad (16)$$

Fitted kinetic parameters are reported in **Supplementary Tables 11-12**. The mean absolute percentage error ($MAPE$) between predicted and measured catalytic performance metrics, q, including X_{CO2}, S_{MeOH}, Y_{MeOH}, or STY_{MeOH}, as defined in **Equation 17**:

$$MAPE_q = \frac{1}{N_{total}} \sum_{N=1}^{N_{total}} \left(\frac{\left|q_{predicted} - q_{measured}\right|}{q_{predicted}} \right)_N \quad (17)$$

Supplementary Table 1. Summary of a Materials Project database search for experimentally reported monoclinic metal oxides with band gaps exceeding 3.5 eV[9].

ID[a]	Formula	Energy above Hull[b] (eV atom^{-1})	Band gap (eV)
mp-2858	ZrO_2	0	3.53
mp-352	HfO_2	0	4.02
mp-1582	As_2O_3	0	4.03
mp-1581	As_2O_3	<0.01	3.63
mp-1194715	As_2O_3	<0.01	3.62
mp-669426	SiO_2	<0.01	5.54
mp-556654	SiO_2	0.01	5.61
mp-1200292	SiO_2	0.02	5.70

[a] Unique Materials Project identifier. [b] Stability metric, where 0 eV atom^{-1} indicates thermodynamic stability.

Supplementary Table 2. Overview of synthesis, nomenclature, composition, and textural properties of mixed binary $InMO_x$ catalysts (M = Hf, Zr).

Catalyst code	Synthesis route[a]	In_2O_3[b] (wt%)	In_2O_3[c] (wt%)	S_{BET}[d] ($m^2\ g^{-1}$)	d_{MOx}[e] (nm)
1$InHfO_x$	FSP	1	0.95	53	13.2
2$InHfO_x$	FSP	2	1.93	51	14.3
3$InHfO_x$	FSP	3	3.10	60	13.2
5$InHfO_x$	FSP	5	5.06	57	17.2
7$InHfO_x$	FSP	7	7.11	52	14.3
10$InHfO_x$	FSP	10	9.89	61	14.3
In_2O_3/HfO_2(P),WI	WI of HfO_2(P)	2	2.21	75	6.4
$InHfO_x$,CP	CP	2	2.14	80	10.7
In_2O_3/HfO_2(FSP),WI	WI of HfO_2(FSP)	2	1.98	69	12.3
HfO_2(P)	P	-	-	81	12.3
HfO_2(FSP)	FSP	-	-	63	13.2
1$InZrO_x$	FSP	1	1.13	102	10.7
2$InZrO_x$	FSP	2	2.04	96	13.2
3$InZrO_x$	FSP	3	3.01	91	9.5
5$InZrO_x$	FSP	5	4.99	95	12.3
7$InZrO_x$	FSP	7	7.19	100	11.5
10$InZrO_x$	FSP	10	9.98	110	12.3
ZrO_2	FSP	-	-	96	12.4
$GaHfO_x$	FSP	2	1.83	58	10.9
$ZnHfO_x$	FSP	2	1.51	55	13.4

[a] Notation: P - precipitation; FSP - flame spray pyrolysis; CP - coprecipitation. [b] Targeted. [c] Determined by ICP-OES. [d] Determined by the BET method. [e] Determined from the Scherrer equation applied to the m-ZrO_2(11−1) or m-HfO_2(11−1) reflections.

Supplementary Table 3. Catalytic performance metrics of the $InHfO_x$ and $InZrO_x$ catalysts in CO_2 hydrogenation.

Catalyst[a]	X_{CO2}[b] (%)	S_{MeOH}[c] (%)	STY_{MeOH}[d] ($g_{MeOH}\ h^{-1}\ g_{In}^{-1}$)	STY_{MeOH}[d] ($g_{MeOH}\ h^{-1}\ g_{cat}^{-1}$)	STY_{MeOH}[d] ($mg_{MeOH}\ h^{-1}\ m_{cat}^{-2}$)
1$InHfO_x$	3.1	31	6.16	0.06	0.95
2$InHfO_x$	4.9	57	9.31	0.15	3.02
3$InHfO_x$	5.8	55	7.69	0.19	3.18
5$InHfO_x$	5.6	83	6.72	0.28	4.87
7$InHfO_x$	7.3	70	5.27	0.31	2.87
10$InHfO_x$	6.8	70	3.37	0.28	4.57
In_2O_3/HfO_2(P),WI	1.4	1	0.00	0.00	0.00
$InHfO_x$,CP	1.6	3	0.00	0.00	0.00
In_2O_3/HfO_2(FSP),WI	3.7	17	2.52	0.04	0.97
HfO_2(FSP)	2.7	1	0.00	0.00	0.00
HfO_2(P)	0.0	0	0.00	0.00	0.00
In_2O_3	5.8	46	0.20	0.17	2.07
1$InZrO_x$	2.4	28	5.51	0.05	0.45
2$InZrO_x$	3.2	44	5.56	0.09	0.91
3$InZrO_x$	4.5	43	5.16	0.13	1.41
5$InZrO_x$	5.7	62	5.14	0.21	2.13
7$InZrO_x$	5.4	64	3.93	0.22	2.28
10$InZrO_x$	6.6	58	3.07	0.25	2.65
ZrO_2	2.9	0	0.00	0.00	0.00

[a] Catalyst overview in **Supplementary Table 1**. [b] CO_2 conversion. [c] Methanol selectivity. [d] Methanol space-time yield normalized per gram of indium, gram of catalyst, or specific surface area, respectively. Reaction conditions: $T = 553$ K, $P = 50$ bar, CO_2:H_2 = 1:4, $GHSV = 24'000\ cm^3\ h^{-1}\ g_{cat}^{-1}$.

Supplementary Table 4. Formation energies (E_f) associated with monoclinic, tetragonal, and cubic HfO_2 and ZrO_2 polymorphs.

Crystal system	Space group	$E_{f,ZrO2}$ (eV f.u.$^{-1}$)	$E_{f,HfO2}$ (eV f.u.$^{-1}$)
monoclinic	$P2_1/c$	–10.39	–10.73
tetragonal	$P4_2/nmc$	–10.28	–10.56
cubic	$Fm\bar{3}m$	–10.19	–10.46

Supplementary Table 5. Surface composition of selected $InHfO_x$ and $InZrO_x$ catalysts.

Catalyst[a]	Form	In/M[b] (at%)	O/M[b] (at%)
HfO_2(P)	fresh	-	2.04
HfO_2(FSP)	fresh	-	1.73
2$InHfO_x$	fresh	0.09	1.83
2$InHfO_x$	equilibrated[c]	0.09	1.73
2$InZrO_x$	fresh	0.06	1.68
2$InZrO_x$	equilibrated	0.06	1.57

[a] Catalyst overview in **Supplementary Table 1**. [b] Determined by XPS. [c] After 20 h under CO_2 hydrogenation, reaction conditions indicated in **Supplementary Table 3**.

Supplementary Table 6. Adsorption energies (E_{ads}) of monomeric and dimeric $In(OH)_3$ species, and aggregation energy (E_{agg}) for the conversion of a monomer into a dimer.

Surface	E_{ads} (eV)		E_{agg} (eV)
	$In(OH)_3$monomer	$In(OH)_3$ dimer	
m-HfO_2	–1.50	–1.04	1.97
m-ZrO_2	–1.30	–0.84	1.76

Supplementary Table 7. Electron paramagnetic resonance (EPR) spectrometer settings.

Experiment (-)	*T* (K)	Microwave frequency (GHz)	Central field (G)	Sweep width (G)	Modulation amplitude[a] (G)	Conversion time (ms)	Time constant (ms)
ex situ	298	9.4	4050	8000	5	81.92	40.96
in situ	298	9.2	3000	5900	3	84.46	40.96
in situ	553	9.2	3000	5900	3	84.46	40.96

[a] Modulation frequency (kHz) and power attenuation (dB) were set to 100 kHz and 20 dB.

Supplementary Table 8. Relative amount of EPR active species in $2InZrO_x$ under distinct working conditions detected via in-situ EPR experiments. The data was fitted using particle swarm optimization method (See **Method**).

Conditions	$V_O^{\bullet}$[a] (%)	Zr^{3+}[a] (%)	O^{2-} (%)
fresh	60	40	0
He	100	0	0
H_2	8	0	92
CO_2	0	0	100
CO_2+H_2	100	0	0

[a] Oxygen vacancy with single electron trapped ($V_O^{\bullet}$) and corresponding reduced metal cation Zr^{3+} upon vacancy generation. See **Supplementary Note 2**.

Supplementary Table 9. Methanol adsorption energies (E_{ads}) over hydroxylated In single atoms anchored on monoclinic and tetragonal HfO_2 or ZrO_2 surfaces.

Model	E_{ads} (eV)
$In(OH)_3$-m-HfO_2	–1.04
$In(OH)_3$-m-ZrO_2	–1.11
$In(OH)_3$-t-ZrO_2	–1.20

Supplementary Table 10. H_2 chemisorption of HfO_2 or ZrO_2 supports prepared by flame spray pyrolysis (FSP).

Support	H_2 uptake ($mm^3\ m^{-2}$)
HfO_2(FSP)	0.81
ZrO_2(FSP)	0.47

Supplementary Table 11. Rate expressions and thermodynamic parameters of the two-site LHHW kinetic model describing methanol (MeOH) and CO (RWGS) formation from CO_2 over the 2InHfO_x and 2InZrO_x catalysts (see **Supplementary Note 4**).

Parameter	Expression	Unit
r_{MeOH}	$k_{MeOH}\frac{\theta_{\#}^2\theta_*}{\sqrt{p_{H_2}}}\left(p_{CO_2}p_{H_2}^3-\frac{p_{CH_3OH}p_{H_2O}}{K_{eq,MeOH}}\right)$	mol s^{-1} kg_{cat}^{-1}
r_{RWGS}	$k_{RWGS}\theta_{\#}\theta_*\left(p_{CO_2}p_{H_2}-\frac{p_{H_2O}p_{CO}}{K_{eq,RWGS}}\right)$	mol s^{-1} kg_{cat}^{-1}
k_{MeOH}	$k_{MeOH,ref}\exp\left(\frac{E_{a,MeOH}}{R}\left(\frac{1}{T_{ref}}-\frac{1}{T}\right)\right)$	mol s^{-1} bar^{-4} kg_{cat}^{-1}
k_{RWGS}	$k_{RWGS,ref}\exp\left(\frac{E_{a,RWGS}}{R}\left(\frac{1}{T_{ref}}-\frac{1}{T}\right)\right)$	mol s^{-1} bar^{-2} kg_{cat}^{-1}
θ_*	$\left(1+K_{CO_2}p_{CO_2}+K_{CO}p_{CO}+K_{CH_3OH}p_{CH_3OH}+K_1K_{CO_2}p_{CO_2}\sqrt{K_{H_2}p_{H_2}}+\frac{K_6K_{CH_3OH}p_{CH_3OH}}{\sqrt{K_{H_2}p_{H_2}}}\right)^{-1}$	-
$\theta_{\#}$	$\left(1+\sqrt{K_{H_2}p_{H_2}}+K_{H_2O}p_{H_2O}\right)^{-1}$	-
$K_{eq,MeOH}$	$\exp\left(39.85+\frac{3.17\times10^3}{T}-9.52\ln(T)+56.77\times10^{-4}T-57.5\times10^{-8}T^2+\frac{64.95\times10^3}{T^2}\right)$	bar^{-2}
$K_{eq,RWGS}$	$\exp\left(18.01-\frac{5.87\times10^3}{T}-1.86\ln(T)+2.70\times10^{-4}T+\frac{58.2\times10^3}{T^2}\right)$	-

Supplementary Table 12. Fitted parameters of the two-site LHHW kinetic model for the $2InHfO_x$ and $2InZrO_x$ catalysts.

Parameter	$2InHfO_x$	$2InZrO_x$	Unit
$K_{MeOH,ref}$	6.01×10^{-5}	3.08×10^{-5}	mol s^{-1} bar^{-4} kg_{cat}^{-1}
$k_{RWGS,ref}$	1.39×10^{-3}	7.71×10^{-4}	mol s^{-1} bar^{-2} kg_{cat}^{-1}
$E_{a,MeOH}$	82	87	kJ mol^{-1}
$E_{a,RWGS}$	124	96	kJ mol^{-1}
K_1	0.269	0.346	-
K_6	0.315	1.07	-
K_{H2}	3.08	3.28	bar^{-1}
K_{CO2}	0.316	0.168	bar^{-1}
K_{CO}	0.090	15.2	bar^{-1}
K_{CH3OH}	16.3	8.02	bar^{-1}
K_{H2O}	3.14	2.71	bar^{-1}

Supplementary Table 13. Summary of chemicals used for catalyst synthesis.

Catalyst[a]	Precursor[b]	Supplier	Purity
HfO_2(FSP)	$Hf(OnBu)_4$	ABCR	95%
$InHfO_x$	In, $Hf(OnBu)_4$	Polymet, ABCR	100%, 95%
HfO_2(P)	$HfCl_4$	Strem	99%
In_2O_3/HfO_2(P),WI	$In(NO)_3$, $HfCl_4$	ABCR, Strem	100%, 99%
$InHfO_x$(CP)	$In(NO)_3$, $HfCl_4$	ABCR, Strem	100%, 99%
In_2O_3/HfO_2(FSP),WI	$In(NO)_3$, $Hf(OnBu)_4$	ABCR, ABCR	100%, 95%
ZrO_2(FSP)	$Zr(OEt)_4$	Polymet, ABCR	97%
$InZrO_x$	In, $Zr(OEt)_4$	Polymet, ACROS	100%, 97%
$GaHfO_x$	Ga, $Hf(OnBu)_4$	Polymet, ABCR	100%, 95%
$ZnHfO_x$	$Zn(EHA)_2$, $Hf(OnBu)_4$	Polymet, ABCR	97%, 95%

[a] Catalyst overview in **Supplementary Table 2**. [b] Metal precursors in the desired molar ratio were dissolved in 2-ethylhexanoic acid and tetrahydrofuran (1/3 mass content).

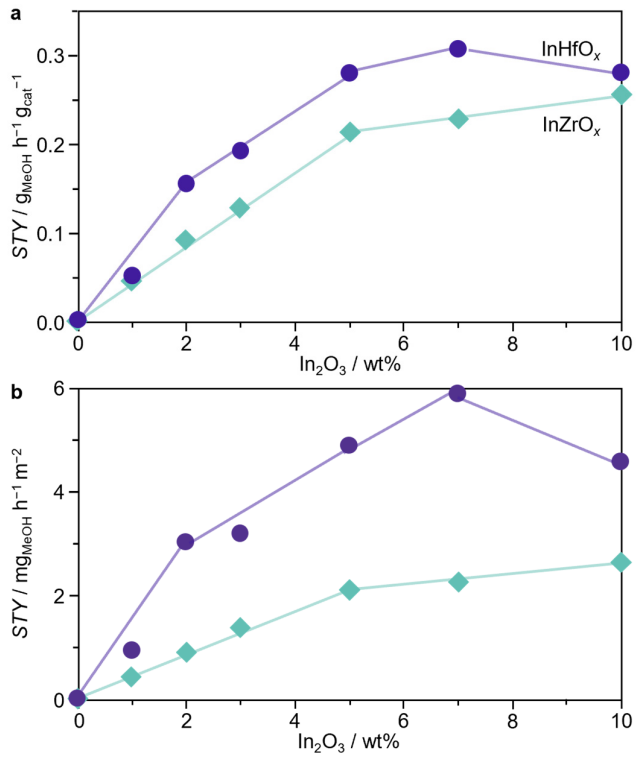

Supplementary Fig. 1. Methanol space-time yield (*STY*) of $InHfO_x$ and $InZrO_x$ catalysts with varying In_2O_3 content, normalized per **a**, gram of catalysts or **b**, specific surface area. Reaction conditions: $T = 553$ K, $P = 50$ bar, $H_2/CO_2 = 4$, $GHSV = 24{,}000$ cm^3 h^{-1} g$_{cat}^{-1}$, $tos = 20$ h.

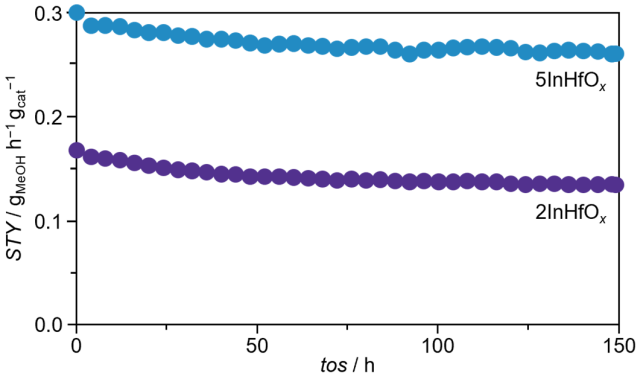

Supplementary Fig. 2. Methanol *STY* versus time on stream (*tos*) over selected $InHfO_x$ catalysts. Reaction conditions: $T = 553$ K, $P = 50$ bar, $H_2/CO_2 = 4$, $GHSV = 24{,}000$ cm^3 h^{-1} g$_{cat}^{-1}$, $tos = 150$ h.

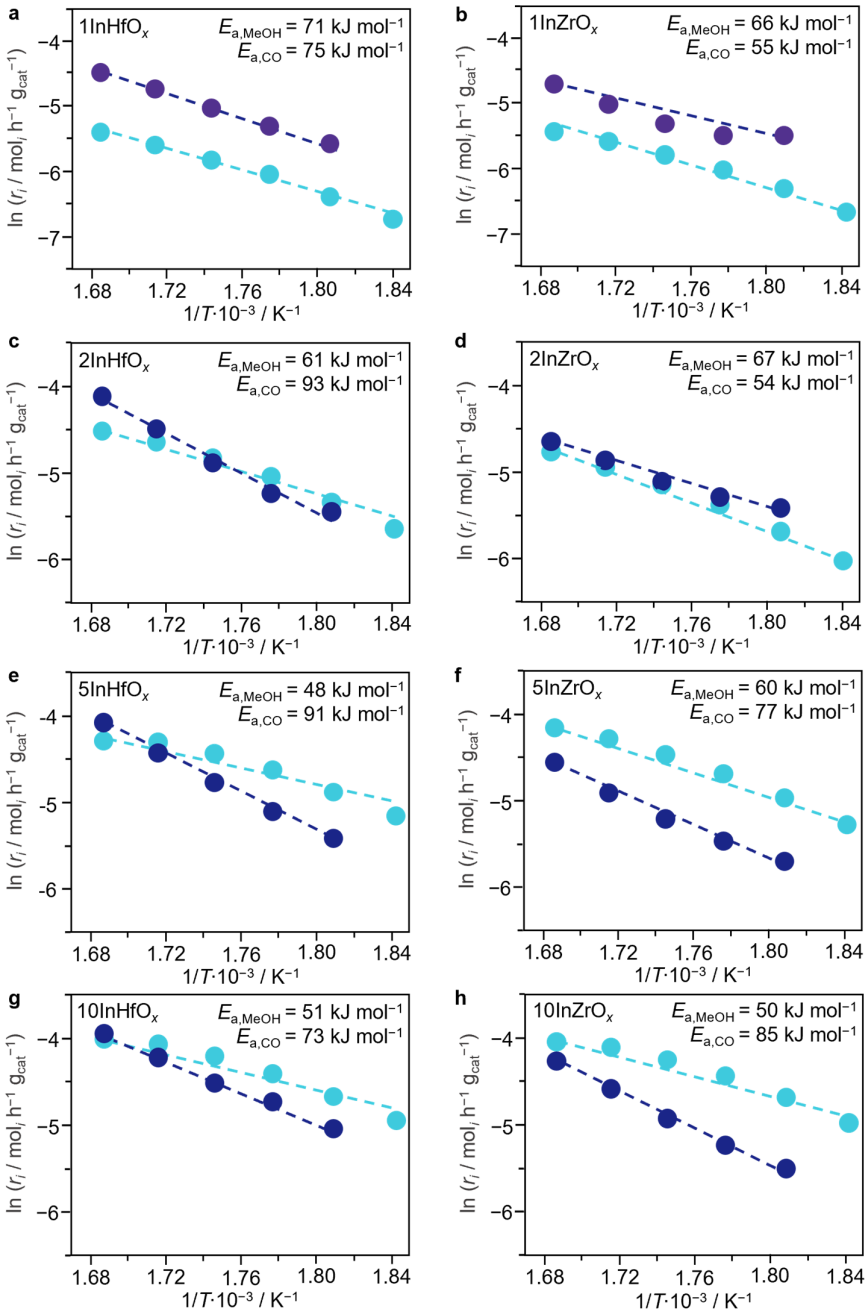

Supplementary Fig. 3. Arrhenius plots used to determine the apparent activation energies for CO_2 hydrogenation to methanol and to CO (RWGS) over selected $InHfO_x$ and $InZrO_x$ catalysts. Reaction conditions: T = 533-593 K, P = 50 bar, H_2/CO_2 = 4, and $GHSV$ = 48,000 cm^3 h^{-1} g$_{cat}^{-1}$.

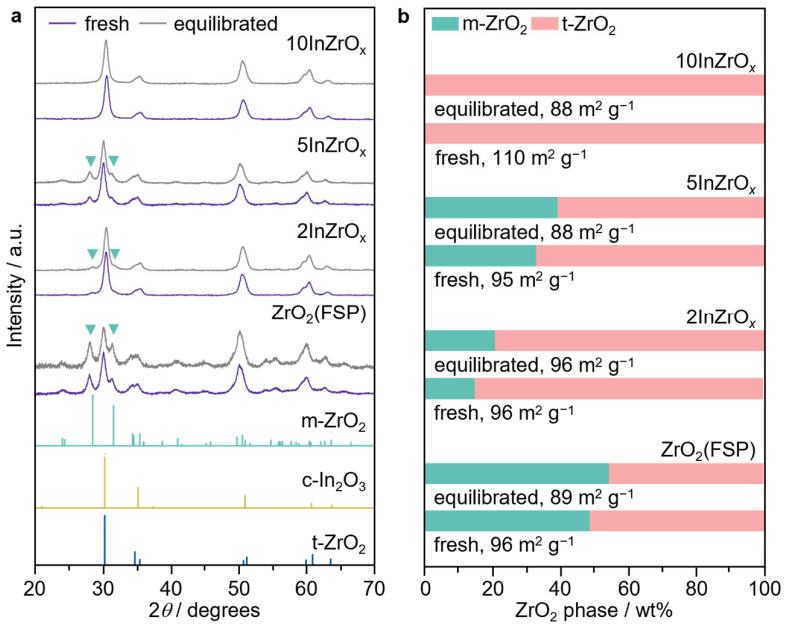

Supplementary Fig. 4. a, XRD patterns of $InZrO_x$ catalysts in fresh (purple lines) and equilibrated (grey lines) forms. **b**, Corresponding phase composition and surface areas of the catalysts. Reaction conditions as indicated in **Supplementary Fig. 1.**

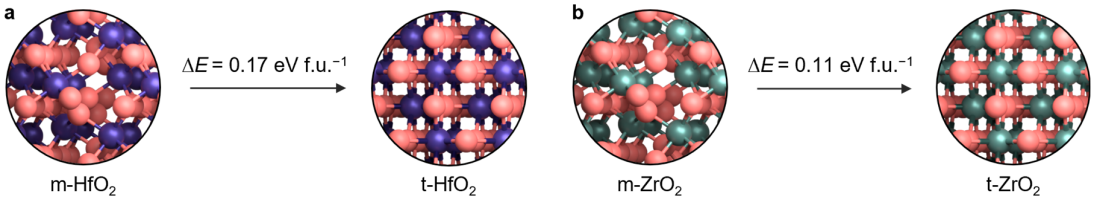

Supplementary Fig. 5. Potential energy difference between monoclinic and tetragonal polymorphs of **a**, HfO_2 and **b**, ZrO_2.

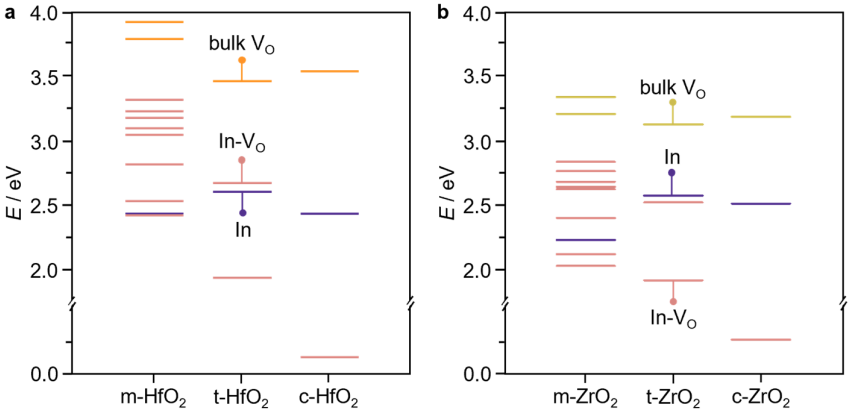

Supplementary Fig. 6. a,**b**, Potential energy of monoclinic (m), tetragonal (t), and cubic (c) in the HfO_2 (**a**) and ZrO_2 (**b**) bulk supercells upon lattice substitution of indium single atom in the presence (In-V_O) or absence (In) of an oxygen vacancy. Oxygen vacancy formation was assessed for all non-equivalent oxygen atoms of undoped systems. For $InMO_x$ models, we explored the vacancy formation for all distinct O coordinated to indium.

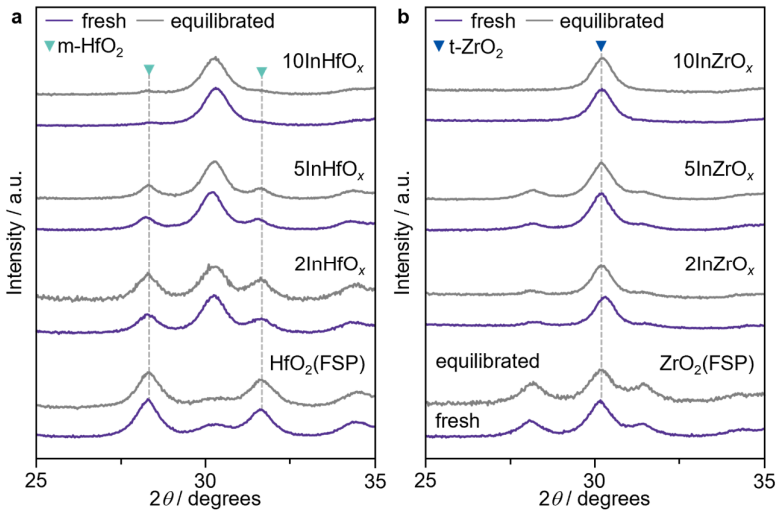

Supplementary Fig. 7. a, XRD patterns of **a**, $InHfO_x$ and **b**, $InZrO_x$ catalysts in fresh (purple lines) and equilibrated (grey lines) forms. The main reflections remain unchanged for both systems, indicating that indium atoms exist on the support surface as isolated sites, patches, or particles. Reaction conditions as indicated in **Supplementary Fig. 1**.

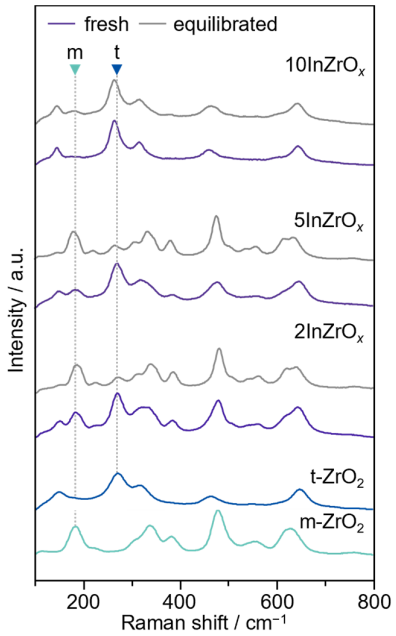

Supplementary Fig. 8. Raman spectra of $InZrO_x$ catalysts in fresh (purple lines) and equilibrated (grey lines) forms. Reaction conditions as indicated in **Supplementary Fig. 1**.

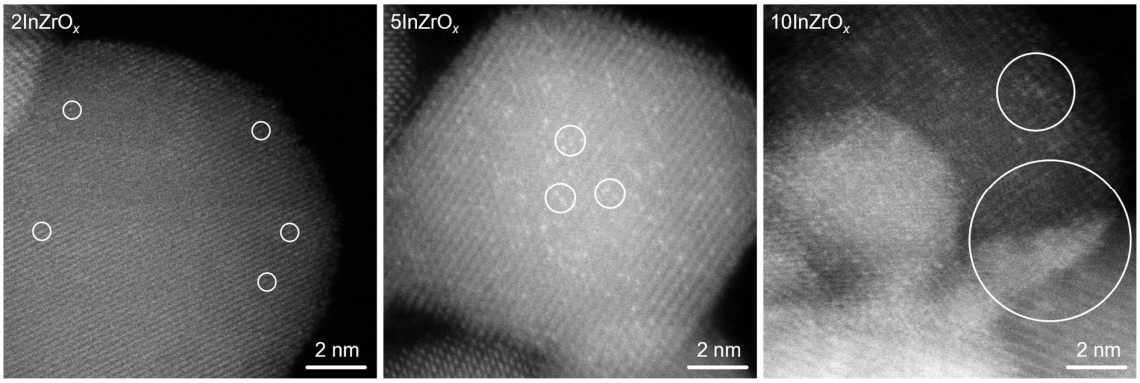

Supplementary Fig. 9. HAADF-STEM images of selected $InZrO_x$ catalysts in fresh form. White circles highlight distinct InO_x species, ranging from isolated single atoms to larger clusters and patches.

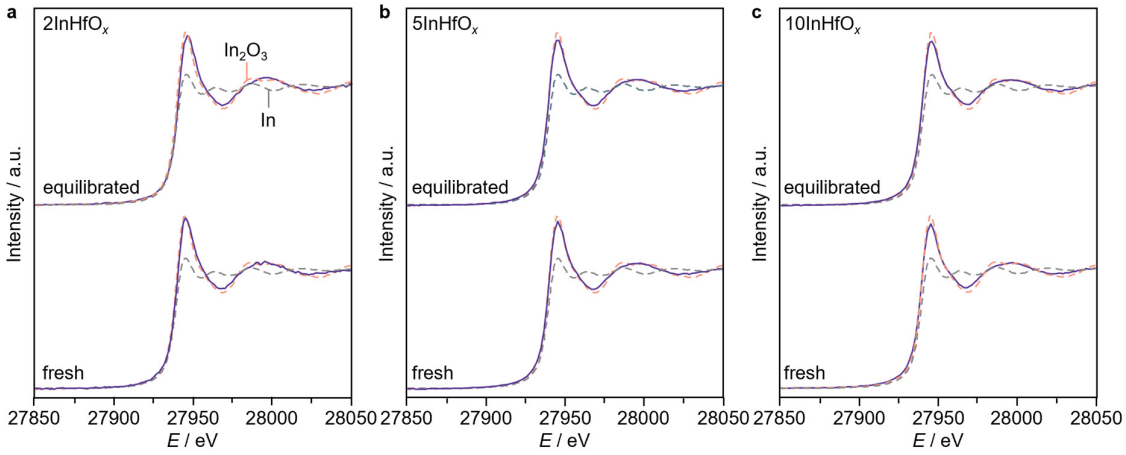

Supplementary Fig. 10. Ex-situ In *K*-edge XANES spectra of **a**, 2InHfO$_x$, **b**, 5InHfO$_x$, and **c**, 10InHfO$_x$ catalysts in fresh and equilibrated forms. Reference spectra of bulk In$_2$O$_3$ and In metal are shown as pink and grey dash lines, respectively.

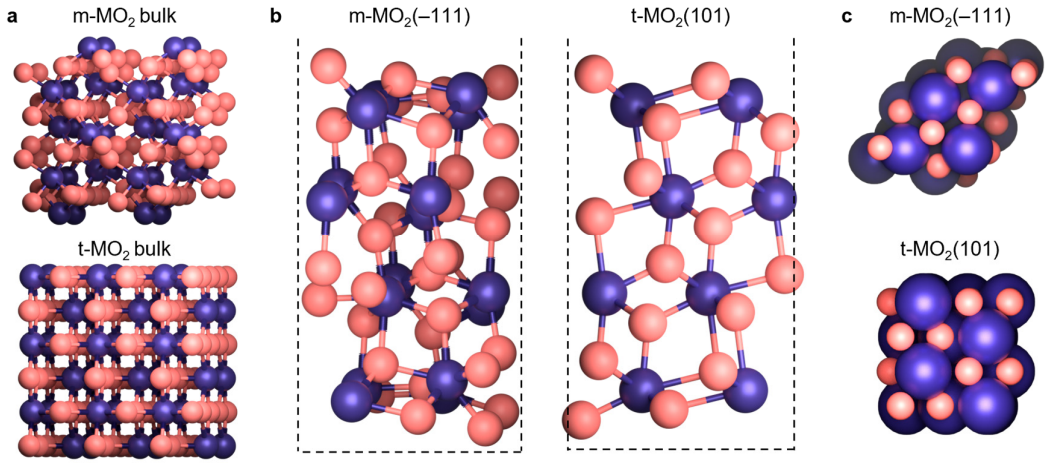

Supplementary Fig. 11. DFT models of **a**, bulk structures, and **b**,**c**, side and top views of m-HfO$_2$ and t-HfO$_2$ slab models used to evaluate the incorporation of single-atom indium species and oxygen vacancy formation. Colour code: Hf - purple; O - salmon pink. Equivalent models for monoclinic and tetragonal ZrO$_2$ were used in the corresponding simulations, differing only in lattice parameters.

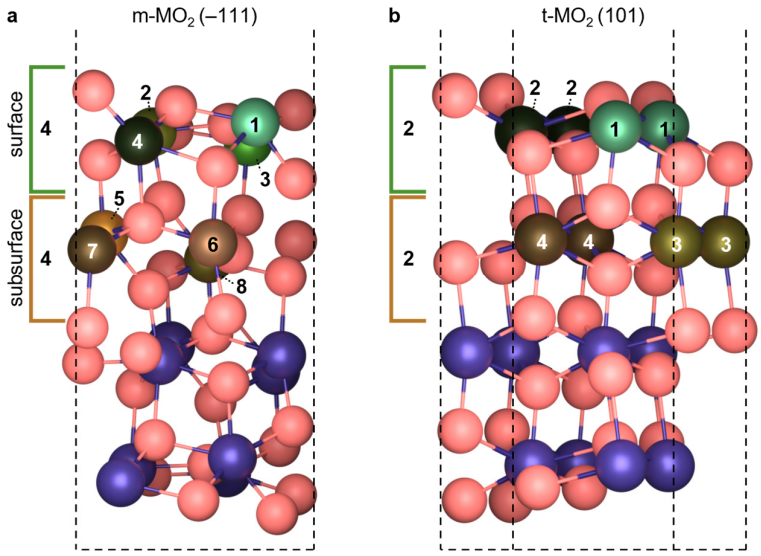

Supplementary Fig. 12. Side view of **a**, m-HfO_2 and **b**, t-HfO_2 slab models used in DFT simulations to assess indium incorporation at all non-equivalent Hf sites. Colour code: Distinct surface and subsurface Hf sites numbered 1-8 - varying shades of green and orange; Hf atoms in bulk positions - dark purple; O atoms - salmon pink. Equivalent models for m-ZrO_2 and t-ZrO_2 were used in the corresponding simulations, differing only slightly in lattice parameters.

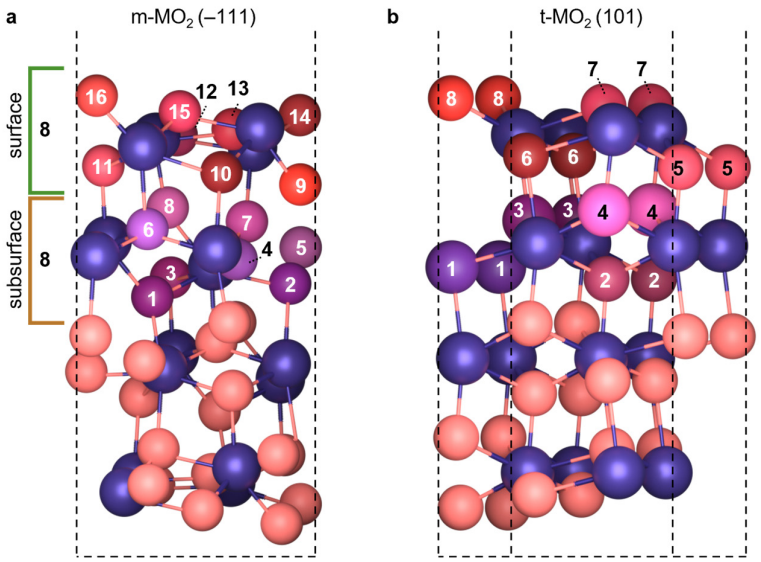

Supplementary Fig. 13. Side views of **a**, m-HfO_2 and **b**, t-HfO_2 slab models used in DFT simulations to evaluate oxygen vacancy formation at all non-equivalent oxygen sites. Colour code: Distinct surface and subsurface O sites numbered 1-16 – distinct red and purple shades; O atoms in bulk positions - salmon pink, Hf atoms - dark purple. Equivalent monoclinic and tetragonal ZrO_2 models were also used, differing only in lattice parameters.

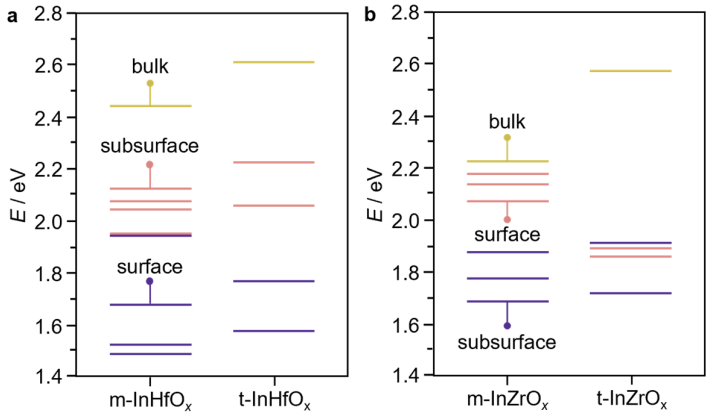

Supplementary Fig. 14. Potential energy of single indium atom substitution into **a**, HfO_2 and **b**, ZrO_2 monoclinic and tetragonal slab models. Indium atoms were substituted at all non-equivalent surface and subsurface Hf or Zr sites, respectively. The energy for substituting an indium atom in the bulk, representing one site per polymorph, is shown for reference.

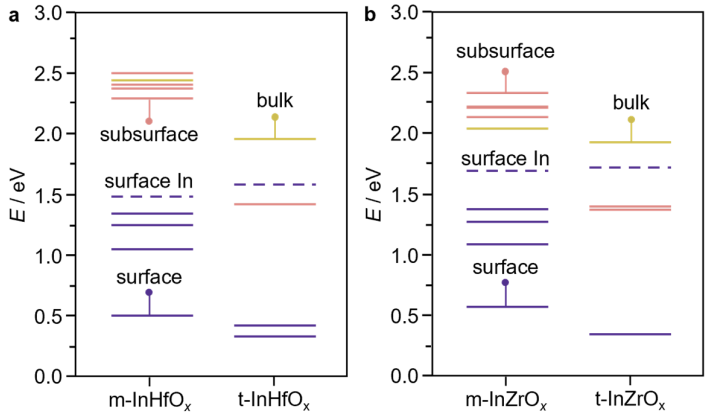

Supplementary Fig. 15. Potential energy of single indium atom substitution into **a**, HfO_2 and **b**, ZrO_2 monoclinic and tetragonal models containing one oxygen vacancy. Indium atoms were substituted into all non-equivalent surface and subsurface Hf or Zr sites, respectively, and oxygen vacancy formation was assessed for all non-equivalent oxygens. The energy of substituting an indium atom in the bulk, representing a single site per polymorph, is shown in yellow, and the lowest energy for substituting an indium atom without a vacancy (**Supplementary Fig. 14**) is shown with dashed lines for reference.

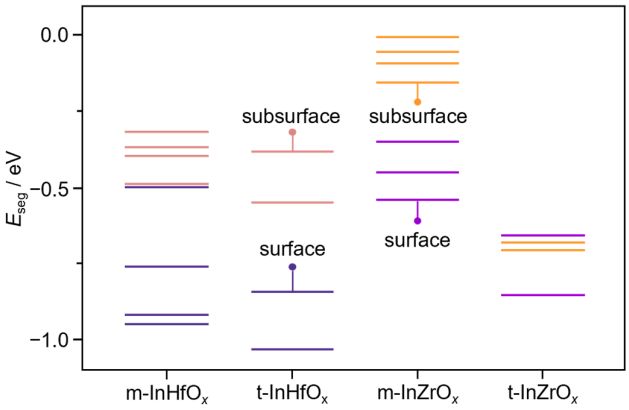

Supplementary Fig. 16. Segregation energies (E_{seg}) for the migration of indium atom from bulk to surface and subsurface sites in distinct tetragonal and monoclinic slab models of HfO_2 and ZrO_2.

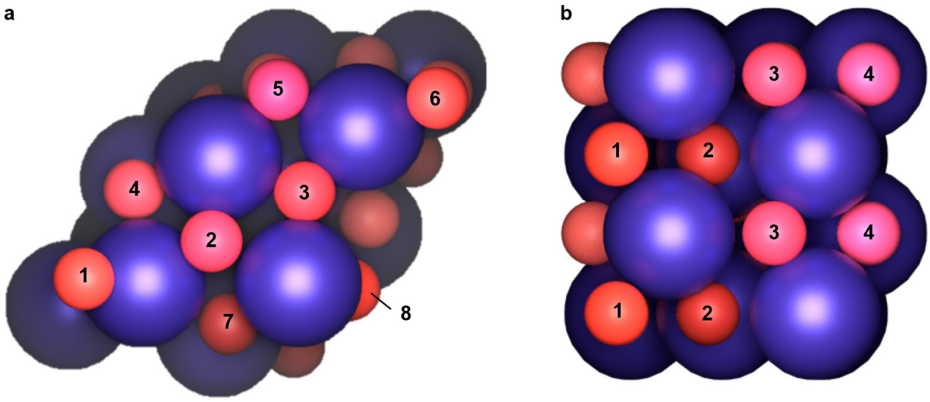

Supplementary Fig. 17. Top view of slab models of **a**, m-HfO_2 and **b**, t-HfO_2 used in DFT simulations to assess the anchoring of In atoms and hydroxylated In adatoms at various surface oxygen sites. Colour code: Distinct surface O sites numbered 1-8 (varying shades of red); M atoms in bulk positions (dark purple); O atoms (salmon pink). Models of monoclinic and tetragonal ZrO_2 are analogous with minor lattice differences.

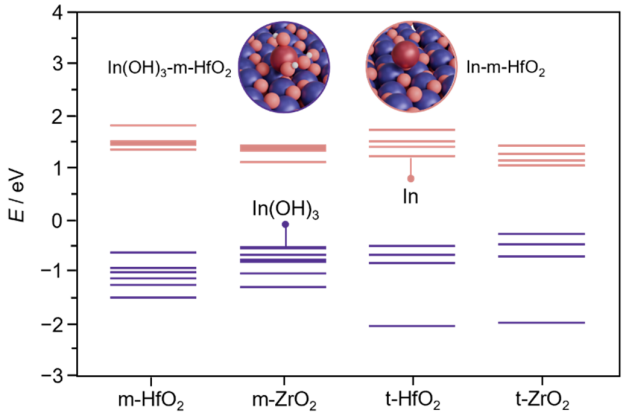

Supplementary Fig. 18. Comparison of adsorption energies of an indium atom and hydroxylated indium adatom on monoclinic and tetragonal HfO_2 and ZrO_2 polymorphs in the non-equivalent positions shown in **Supplementary Fig. 17**.

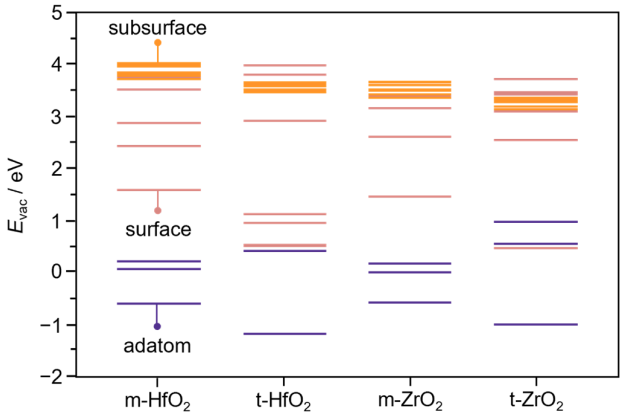

Supplementary Fig. 19. Vacancy formation energy (E_{vac}) of a single oxygen vacancy for monoclinic and tetragonal HfO_2 and ZrO_2 models with $In(OH)_3$ adsorbed. Vacancy formation was explored for all non-equivalent oxygens in the surface/subsurface, as well as at three sites corresponding to the hydroxyl oxygen atoms of the adsorbed species.

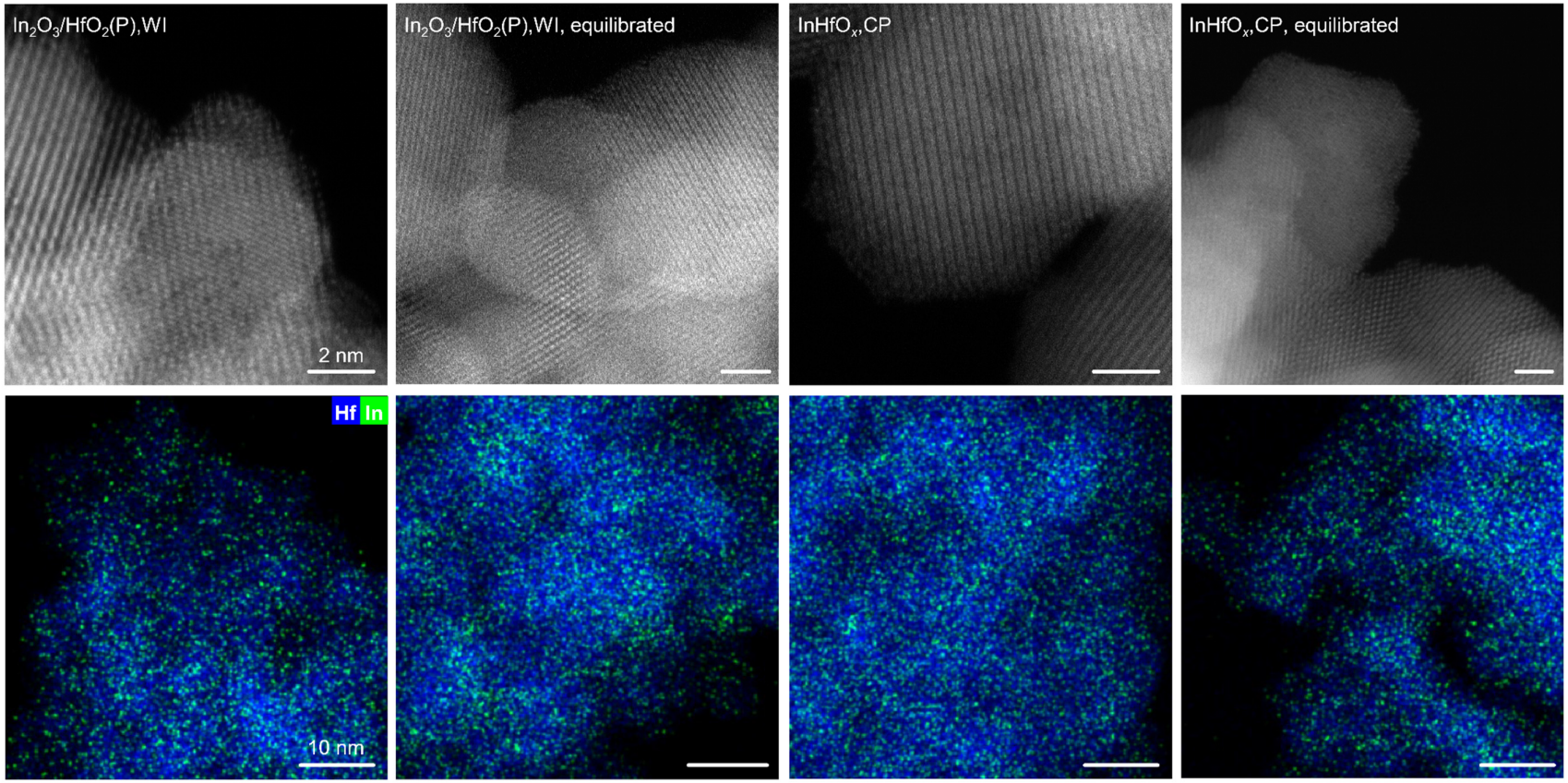

Supplementary Fig. 20. Representative HAADF-STEM images (top) and corresponding elemental maps (bottom) of In_2O_3/HfO_2(P),WI and $InHfO_x$,CP in fresh and equilibrated forms. The results confirm atomic dispersions of InO_x species in all cases. Catalyst codes as reported in **Supplementary Table 2**. Reaction condition as described in **Supplementary Fig. 1**.

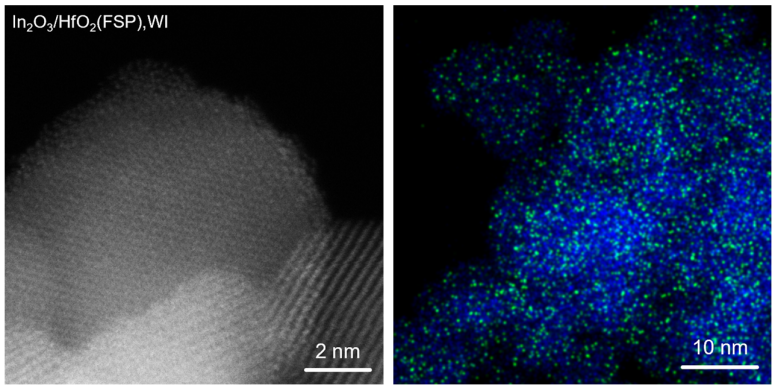

Supplementary Fig. 21. HAADF-STEM image (left) and corresponding elemental map (right) of In_2O_3/HfO_x(FSP),WI in fresh and equilibrated forms. Reaction conditions as described in **Supplementary Fig. 1**.

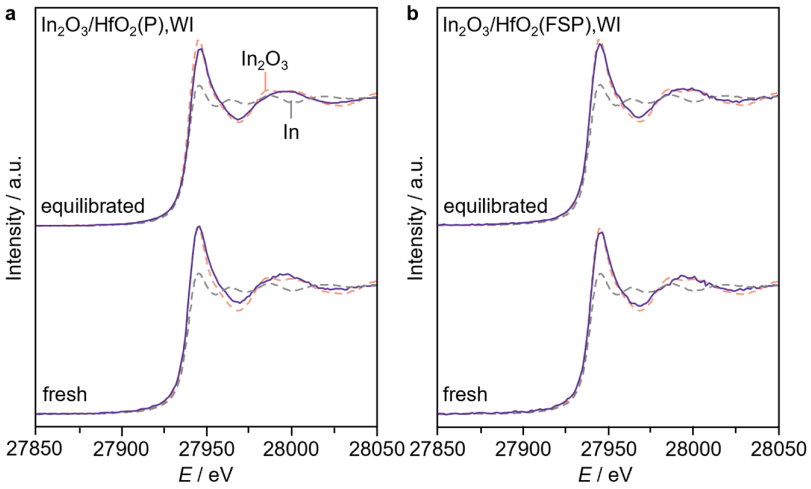

Supplementary Fig. 22. Ex-situ In *K*-edge XANES spectra of **a**, In_2O_3/HfO_2(P),WI and **b**, In_2O_3/HfO_2(FSP),WI catalysts in fresh and equilibrated forms. Reference spectra of bulk In_2O_3 and In metal are shown with orange and grey dash lines, respectively. Reaction conditions as described in **Supplementary Fig. 1**.

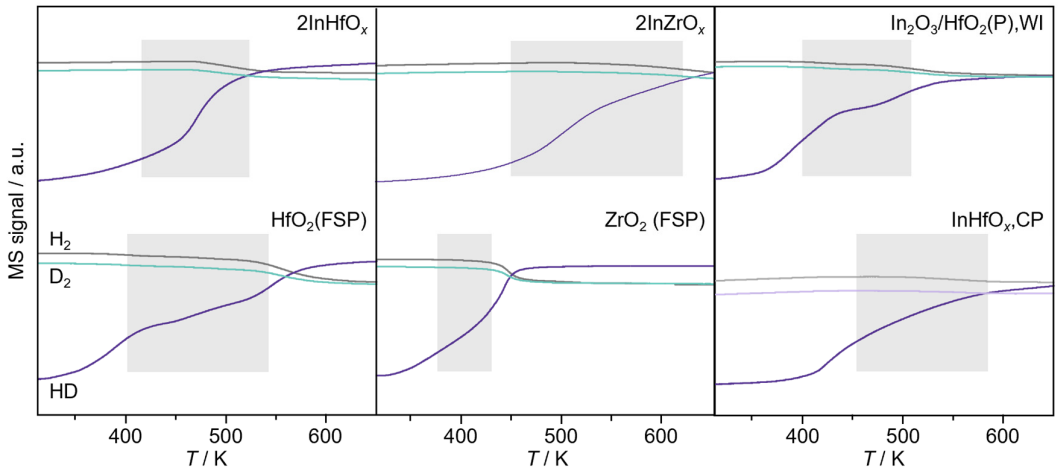

Supplementary Fig. 23. Temperature-programmed H_2-D_2 exchange profiles of selected catalysts. Shaded areas indicate temperature ranges where isotopic exchange occurs. Corresponding profiles of the bare supports are shown for comparison.

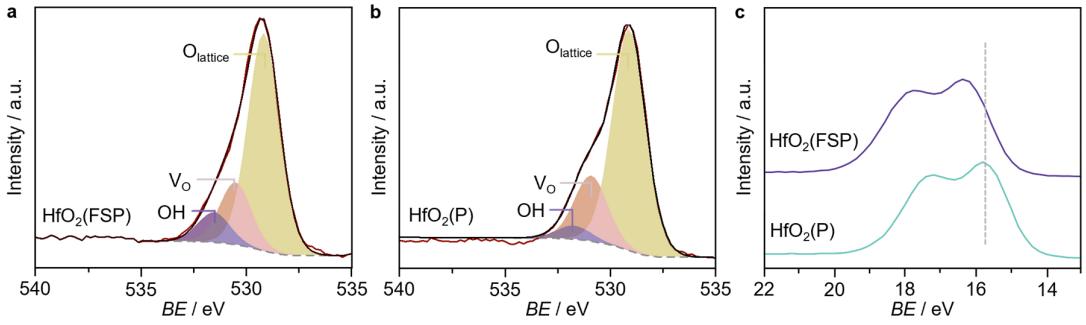

Supplementary Fig. 24. XPS O 1*s* core-level spectra for **a**, HfO_2(FSP) and **b**, HfO_2(P) highlighting differences in oxygen coordination environments. **c**, XPS Hf 4*f* core-level spectra of both samples.

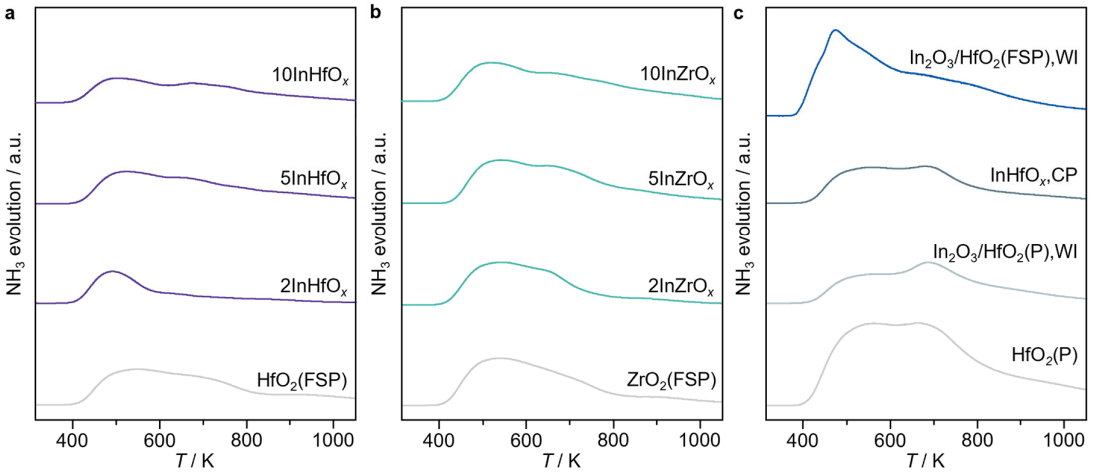

Supplementary Fig. 25. NH_3-TPD profiles of **a**, $InHfO_x$ catalysts, and reference **b**, $InZrO_x$ catalysts, and **c**, HfO_2-supported systems. The profiles of the pure supports are shown for reference.

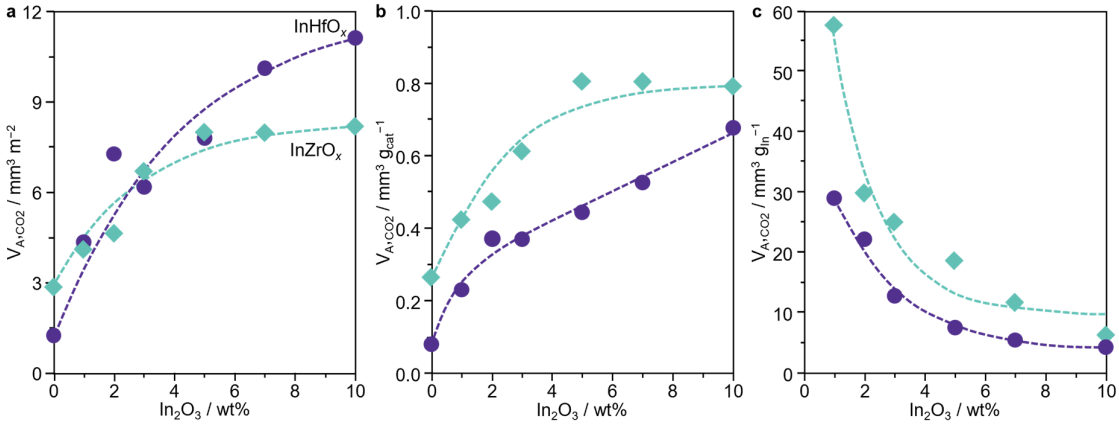

Supplementary Fig. 26. Volumetric CO_2 uptake of $InHfO_x$ and $InZrO_x$ catalysts normalized by **a**, specific surface area, **b**, catalyst mass, and **c**, indium content.

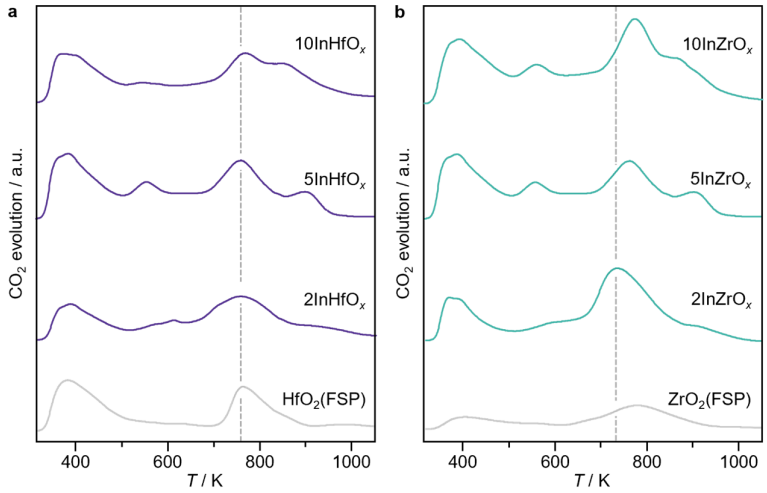

Supplementary Fig. 27. CO_2-TPD profiles of **a**, $InHfO_x$ and **b**, $InZrO_x$ catalysts. Grey lines show the profiles of the corresponding pure support. Vertical dashed lines mark the change of the position of high-temperature desorption peaks.

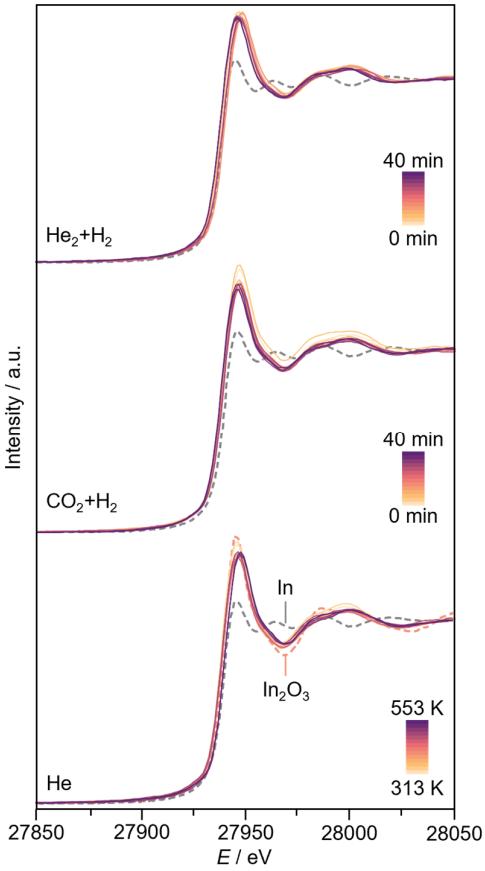

Supplementary Fig. 28. Operando In *K*-edge XANES spectra of $2InZrO_x$ (m_{cat} = 0.013 g) during heating in He (rate = 5 K min^{-1}, F_T = 20 cm^3 min^{-1}, T = 553 K, P = 15 bar, dwell time = 60 min), under CO_2+H_2 (F_T = 20 cm^3 min^{-1}, T = 553 K, P = 15 bar, H_2/CO_2 = 4, dwell time = 60 min), and under He+H_2 (F_T = 20 cm^3 min^{-1}, T = 553 K, P = 15 bar, H_2/He = 4, dwell time = 60 min).

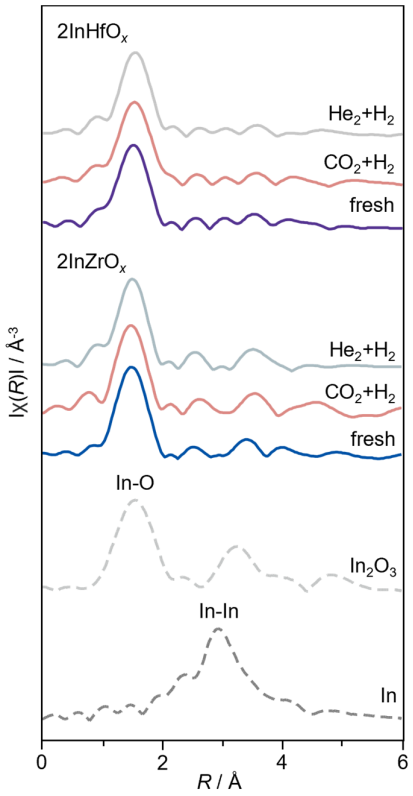

Supplementary Fig. 29. Operando In *K*-edge EXAFS spectra of 2InHfO$_x$ and 2InZrO$_x$ in fresh form and during treatment in CO_2+H_2 or He+H_2 mixtures. The spectra of bulk In and In_2O_3 are shown for reference.

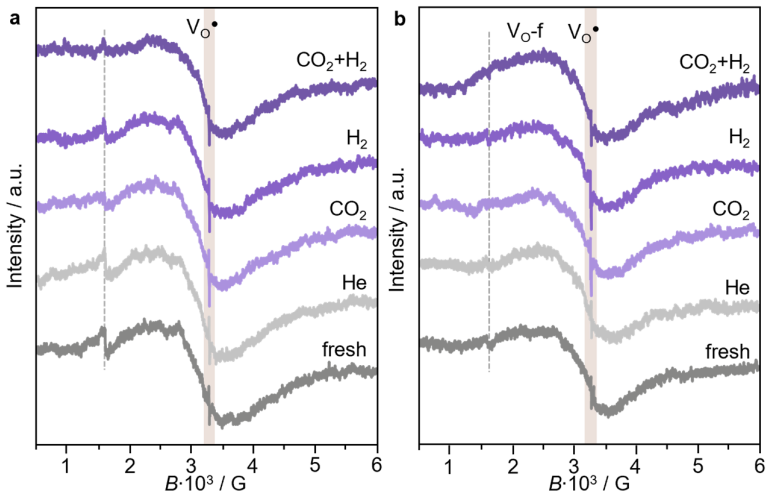

Supplementary Fig. 30. a,**b**, Full in-situ EPR spectra for 2InHfO_x (**a**) and 2InZrO_x (**b**) catalysts, recorded at room temperature and during heating in He (F_T = 210 cm^3 min^{-1}, heating rate = 50 K min^{-1}, T = 553 K, P = 10 bar), after reducing in H_2 (F_T = 210 cm^3 min^{-1}, T = 553 K, P = 10 bar), after exposing to CO_2 (F_T = 110 cm^3 min^{-1}, T = 553 K, P = 10 bar), and after CO_2 hydrogenation (F_T = 200 cm^3 min^{-1}, T = 553 K, P = 10 bar, H_2/CO_2 = 4). The broad signal, attributed to unpaired electrons delocalized over several oxygen vacancies that interact (exchange-coupled vacancy polarons, V_O-f), varies under distinct conditions for 2InZrO_x, being most prominent under CO_2+H_2. The dashed lines indicate the linewidth of V_O-f in the fresh catalysts.

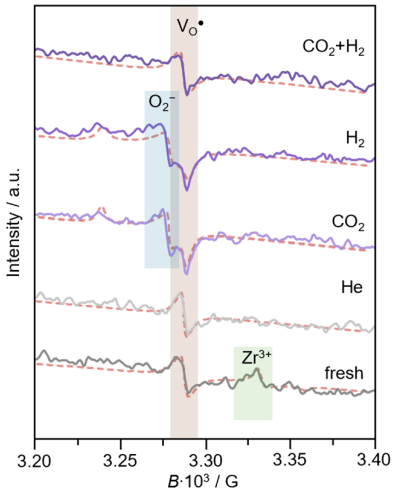

Supplementary Fig. 31. Zoomed-in spectrum of $2InZrO_x$ showing reduced Zr^{3+} species in the fresh state and the emergence of superoxide (O^{2-}) signals under reaction and reducing conditions. The dash lines denote the fitted results using particle swarm optimization method.

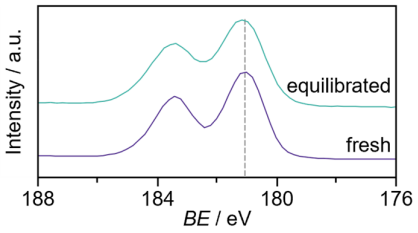

Supplementary Fig. 32. XPS Zr 3*d* core-level spectra of the $2InZrO_x$ catalyst in fresh and equilibrated forms. Reaction conditions as described in **Supplementary Fig. 1**.

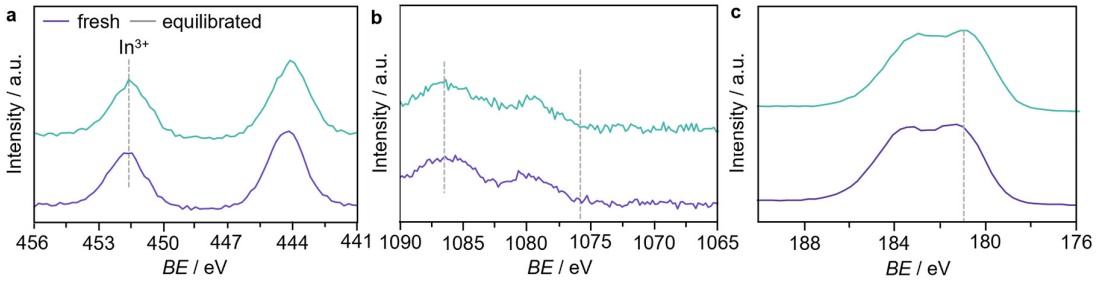

Supplementary Fig. 33. a, In 3*d* and **b**, In MNN XPS spectra of fresh and equilibrated 5InHfO$_x$ catalysts. **c**, Hf 4*f* XPS core-level spectra of 5InHfO$_x$ catalyst.

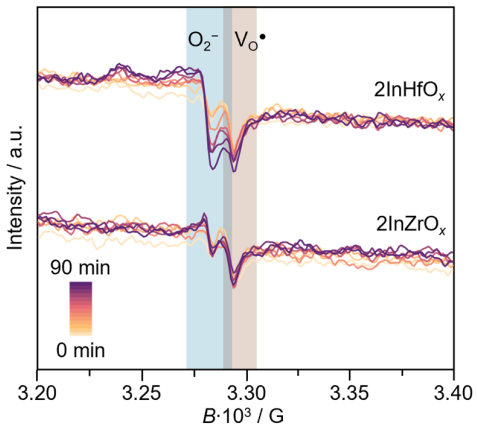

Supplementary Fig. 34. Paramagnetic signals from EPR spectroscopy of 2InHfO$_x$ and 2InZrO$_x$ catalysts following in-situ measurement and exposure to air. Highlighted regions indicate superoxide (O^{2-}) signals, evidencing the presence of surface electrons, with a stronger signal for 2InHfO$_x$.

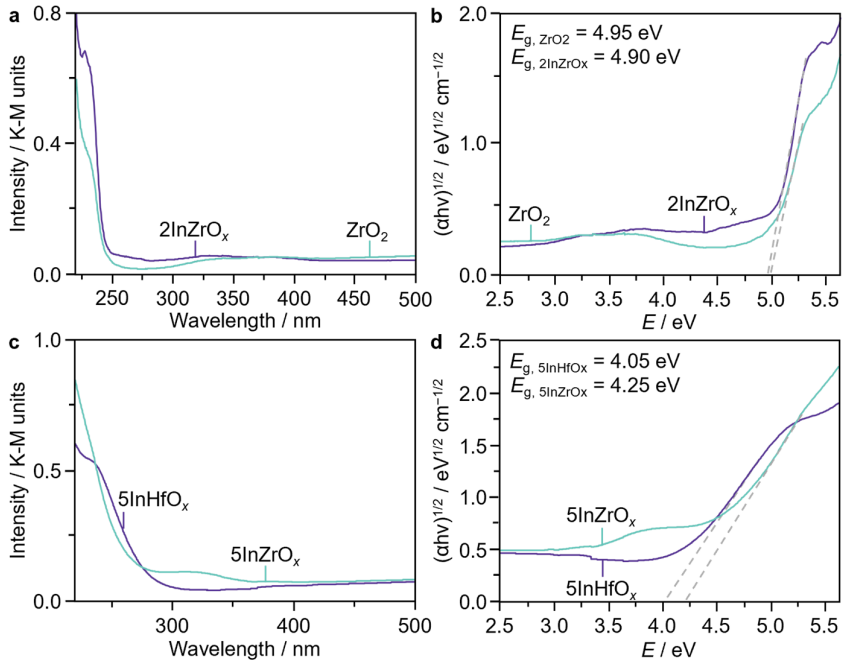

Supplementary Fig. 35. DR-UV-vis spectra of **a**, ZrO_2 and $2InZrO_x$ catalyst and **b**, $5InHfO_x$ and $5InZrO_x$ catalysts. **c**,**d**, Corresponding Tauc plots for bandgap determination.

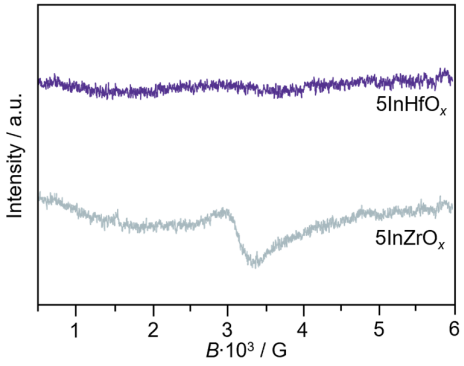

Supplementary Fig. 36. Ex-situ EPR spectra of $5InHfO_x$ and $5InZrO_x$ catalysts. Broad ferromagnetic signals in $5InZrO_x$ arise from electron hopping between oxygen vacancies and Zr 3*d* orbitals. For $5InHfO_x$, these signals are further broadened and suppressed since the energy level of oxygen vacancies overlaps with the conduction band, allowing electron transitions to Hf 4*f* orbitals, indicative of greater electronic coupling.

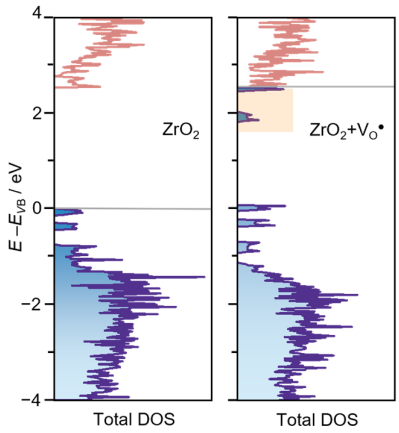

Supplementary Fig. 37. Density of states (DOS) for pristine m-ZrO_2 and m-ZrO_2 with one vacancy. The DOS are aligned with respect to the valence band of the pristine system. The valence band is marked in grey, with the states arising from excess electrons highlighted with red dotted circles. Upon oxygen vacancy formation, electronic states appear in the band gap and near the conduction band, which are associated with the formation of a Zr^{3+} and one electron stored in the oxygen vacancy, respectively.

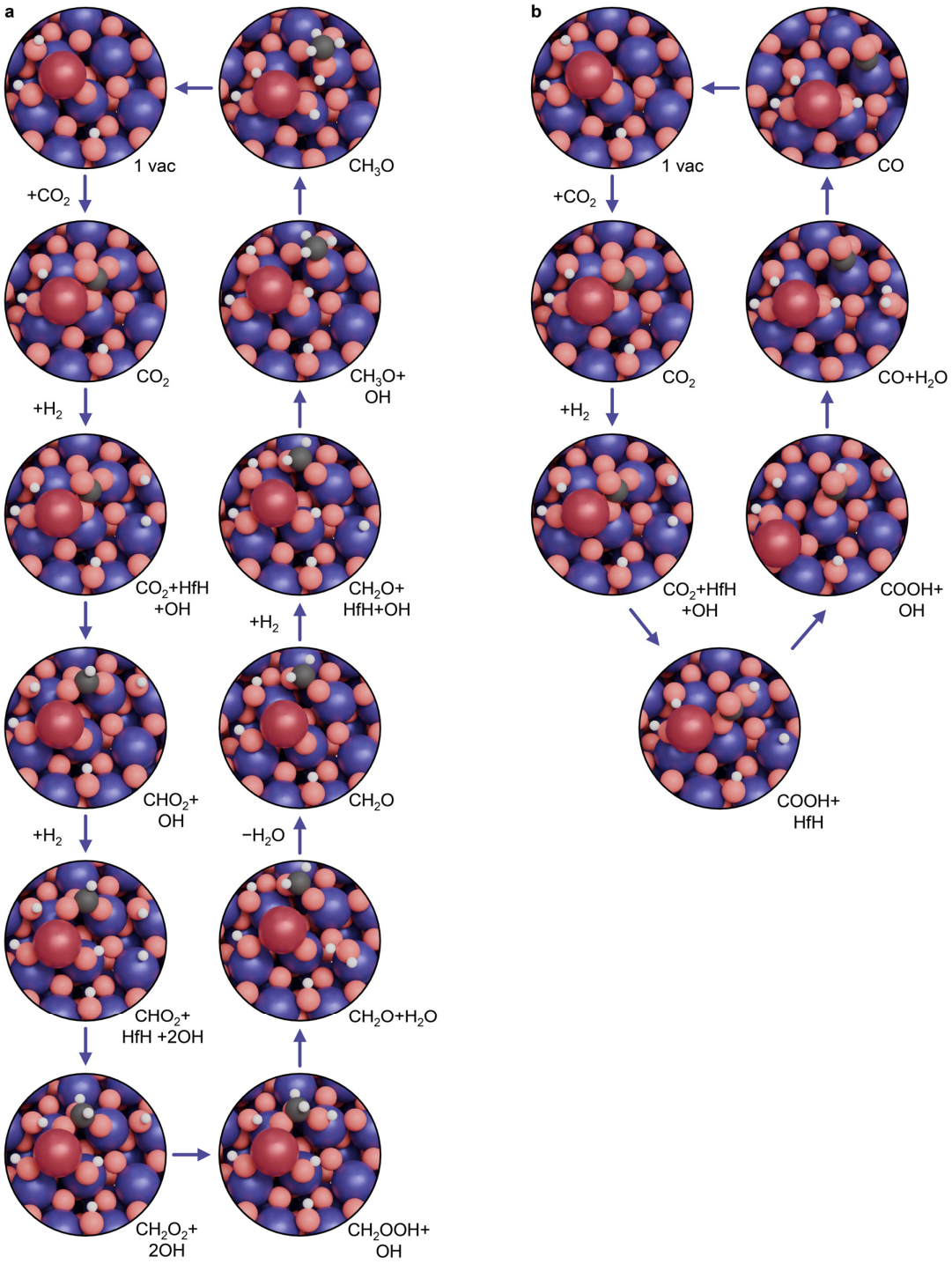

Supplementary Fig. 38. Simulated intermediates for CO_2 conversion to **a**, methanol and **b**, CO over $In(OH)_3$-m-HfO_2 containing one vacancy. Colour code: Hf - purple; In - red; O - salmon pink; C - dark-grey; H - white.

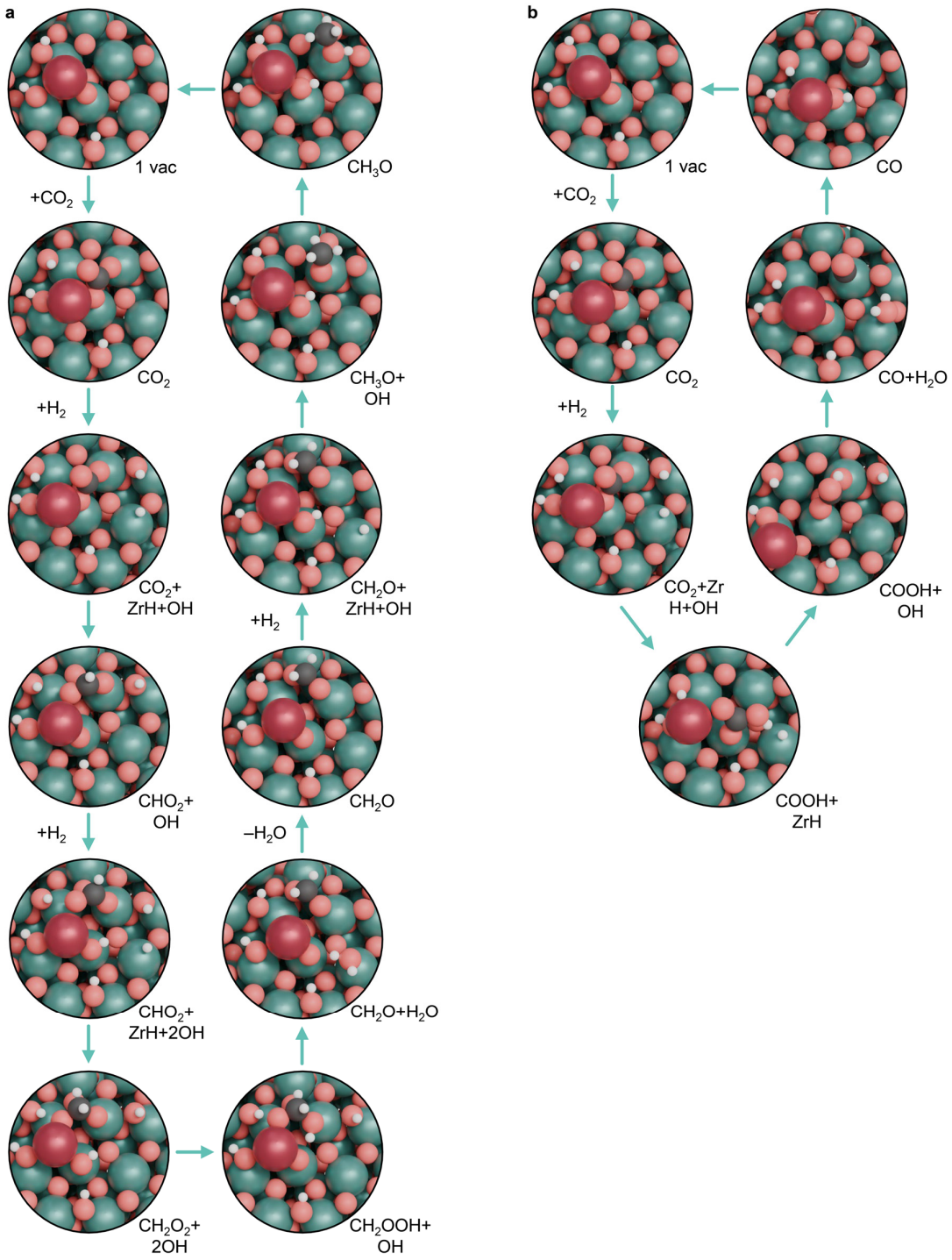

Supplementary Fig. 39. Simulated intermediates for CO_2 conversion to **a**, methanol and **b**, CO over $In(OH)_3$/m-ZrO_2 containing one vacancy. Colour code: Hf - purple; In - red; O - salmon pink; C - dark grey; H - white.

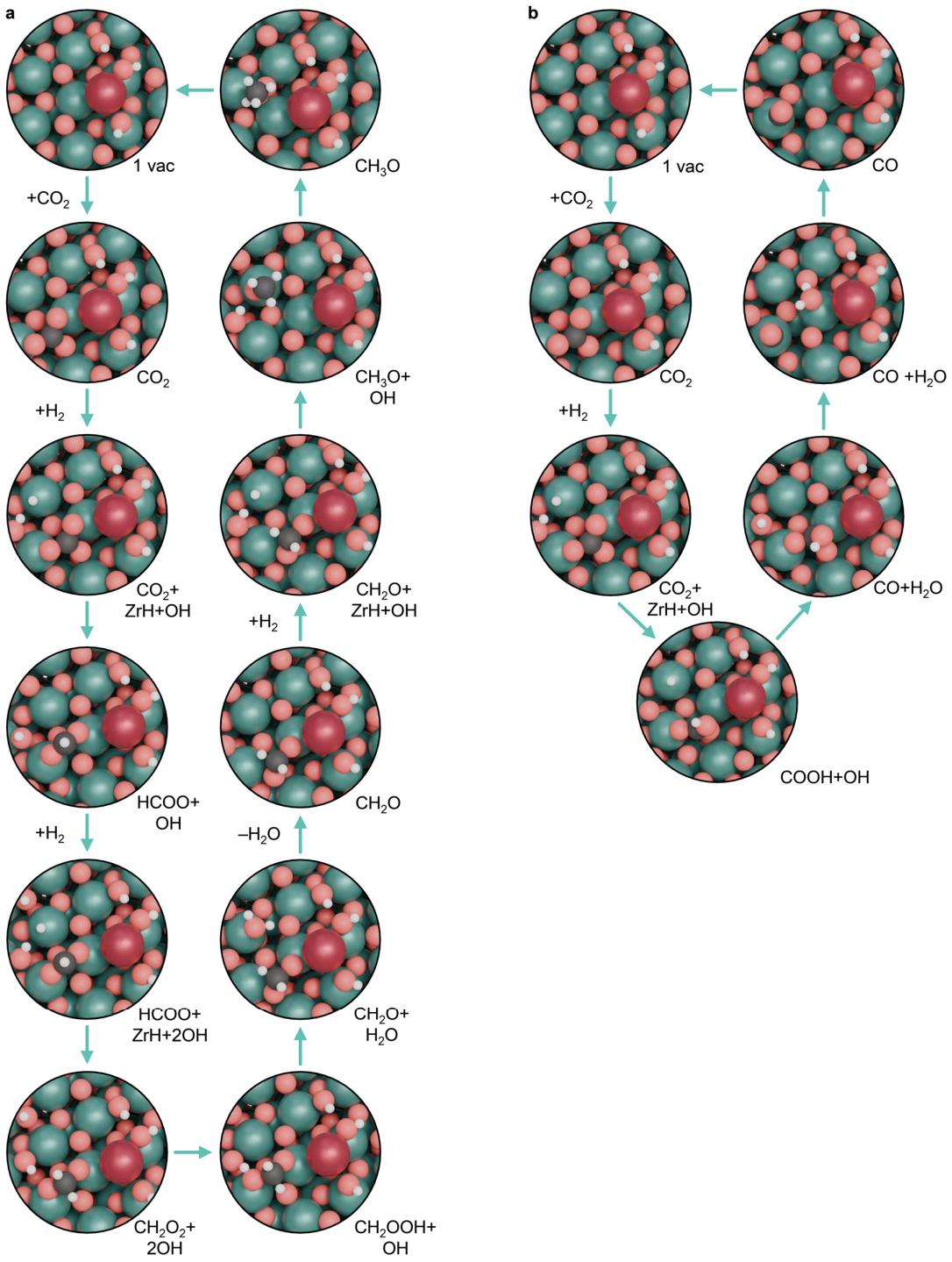

Supplementary Fig. 40. Simulated intermediates for CO_2 conversion to **a**, methanol and **b**, CO over $In(OH)_3$/t-ZrO_2 containing one vacancy. Colour code: Hf - purple; In - red; O - salmon pink; C - dark grey; H - white.

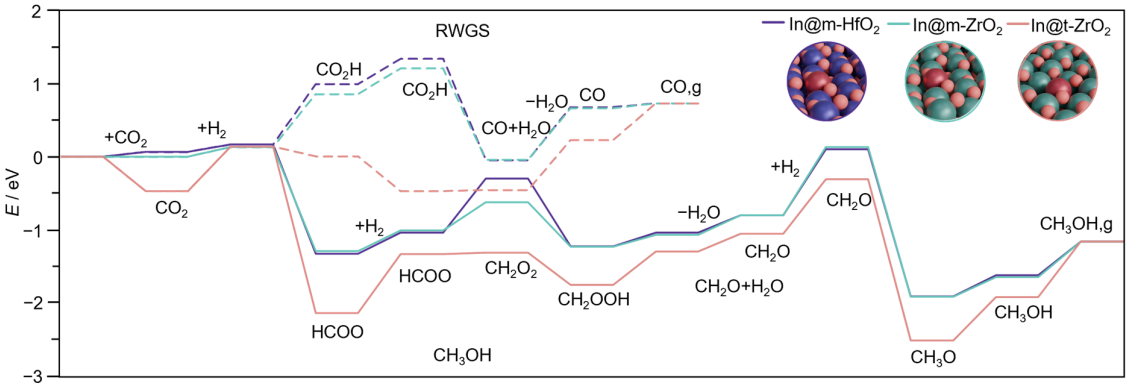

Supplementary Fig. 41. Thermodynamics of reaction paths for CO_2 hydrogenation to methanol (solid lines) and the competing RWGS reactions (dashed line), on m-HfO_2, m-ZrO_2, and t-HfO_2 models containing an incorporated In atom and one oxygen vacancy.

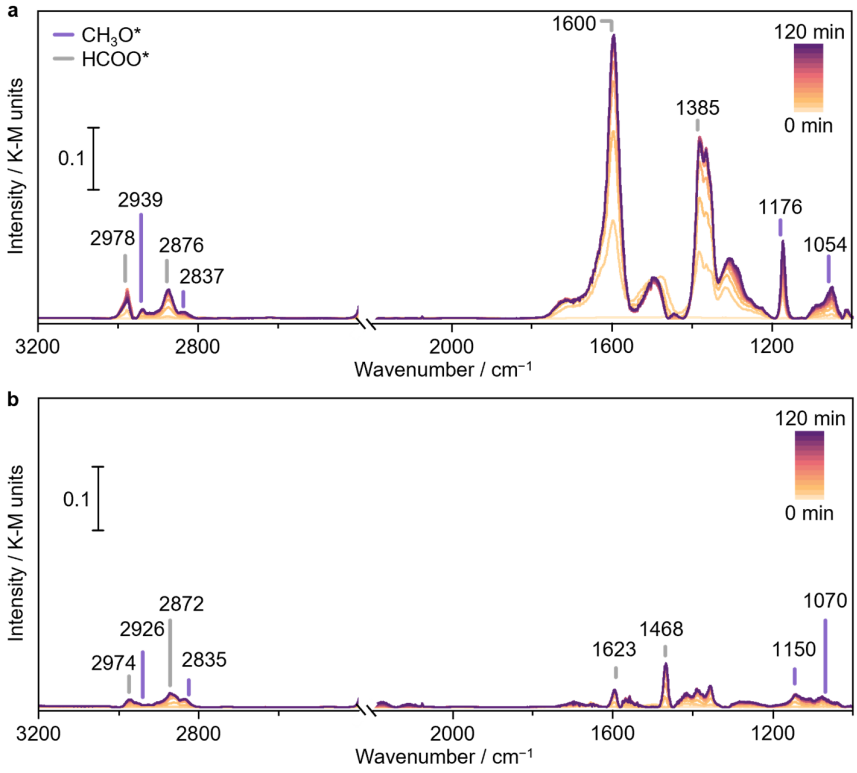

Supplementary Fig. 42. In-situ DRIFT spectra of **a**, 2InHfO_x and **b**, 2InZrO_x under CO_2 hydrogenation conditions (F_T = 20 cm^3 min^{-1}, T = 553 K, P = 20 bar, H_2/CO_2 = 4, dwell time = 120 min).

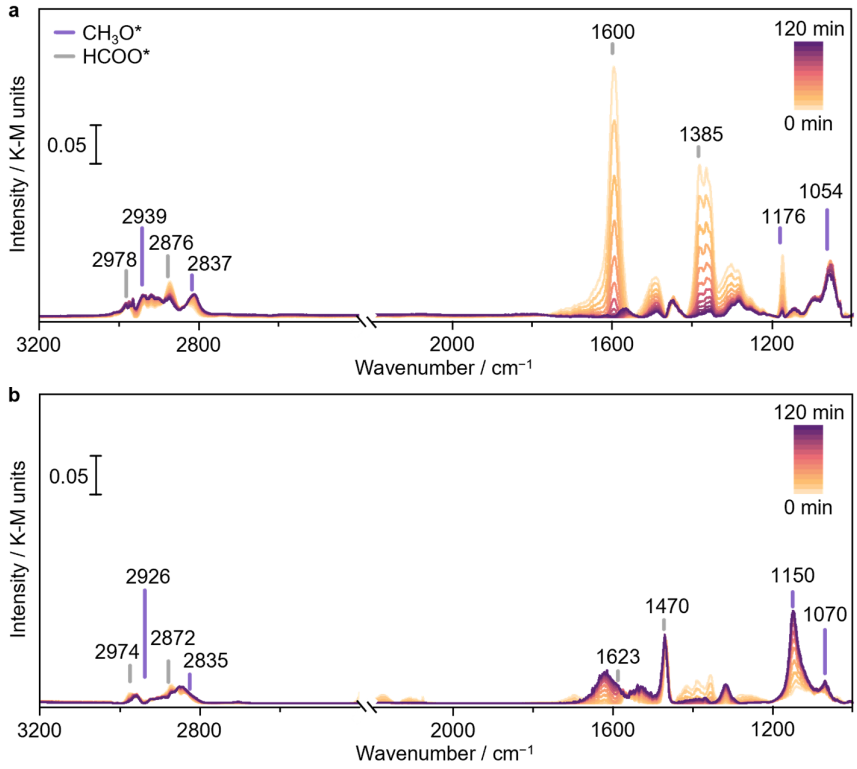

Supplementary Fig. 43. In-situ DRIFT spectra of **a**, 2InHfO_x and **b**, 2InZrO_x after switching to H_2 balanced with He ($F_T = 20$ cm^3 min^{-1}, $T = 553$ K, $P = 20$ bar, H_2/He = 4, dwell time = 120 min).

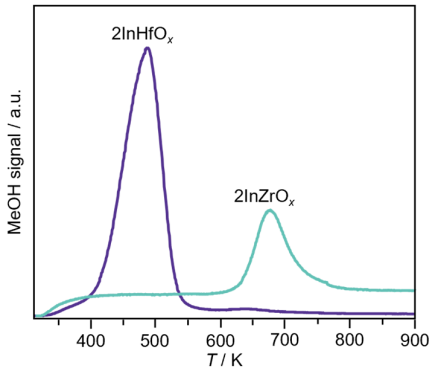

Supplementary Fig. 44. MeOH-TPD profiles of fresh 2InHfO_x and 2InZrO_x catalysts.

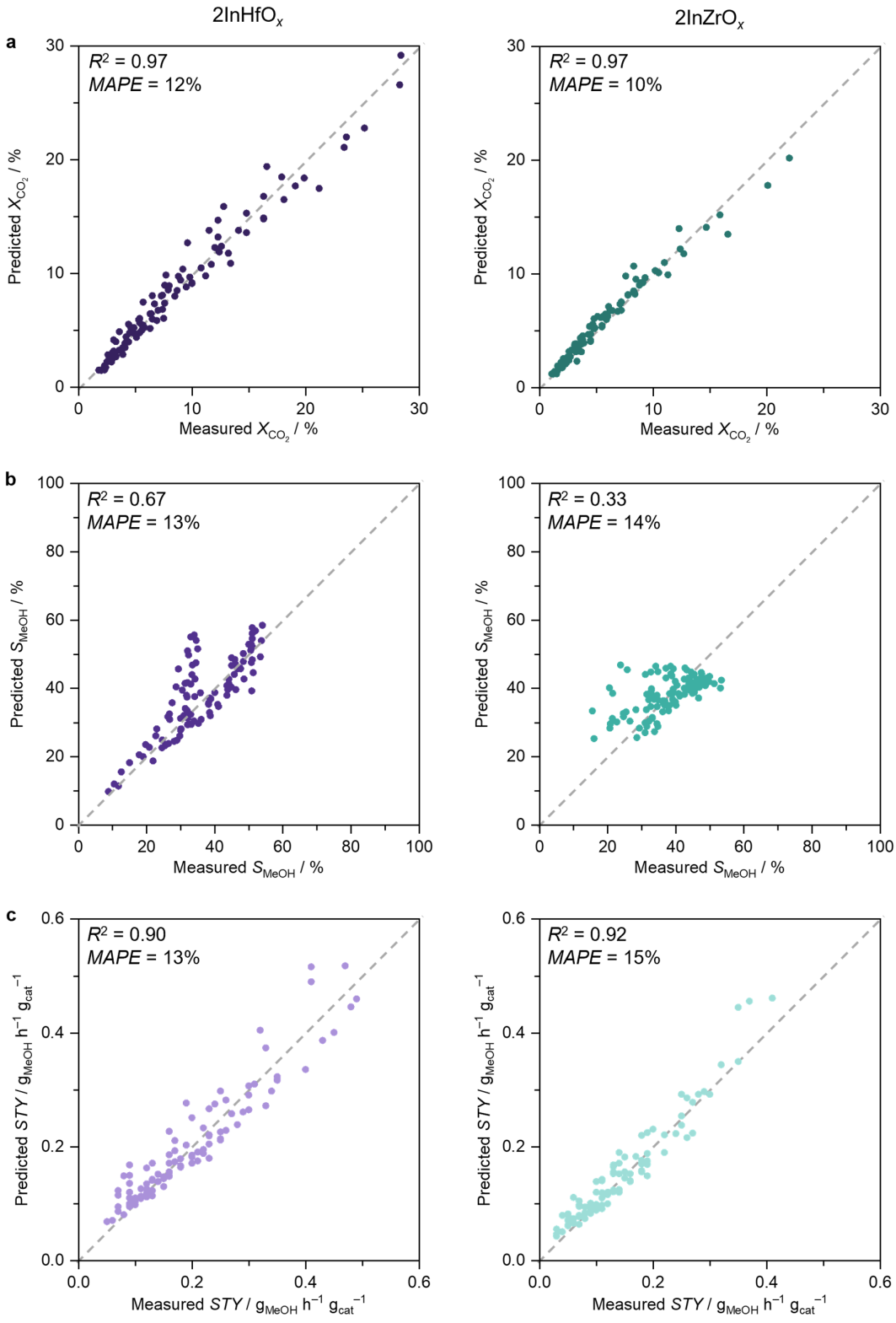

Supplementary Fig. 45. Parity plots comparing **a**, X_{CO2}, **b**, S_{MeOH}, **c**, *STY* during CO_2 hydrogenation over 2InHfO_x (left) and 2InZrO_x (right) predicted by the two-site LHHW kinetic model (**Supplementary Table 9**) versus experimental data. Mean absolute percentage errors

(*MAPE*) and coefficients of determination (R^2) are provided for each metric. Dashed lines indicate the identity line ($x = y$).

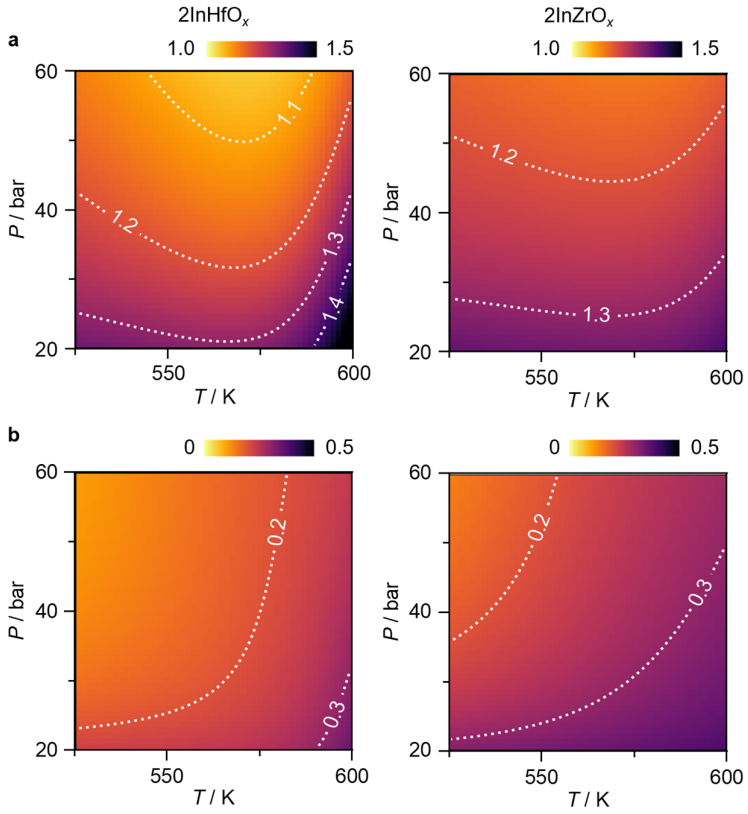

Supplementary Fig. 46. Apparent reaction orders with respect to **a**, H_2 and **b**, CO_2 for methanol formation as a function of T and P at $GHSV$ = 24,000 cm^3 h^{-1} g$_{cat}^{-1}$, for 2InHfO$_x$ and 2InZrO$_x$ as calculated by the kinetic model.

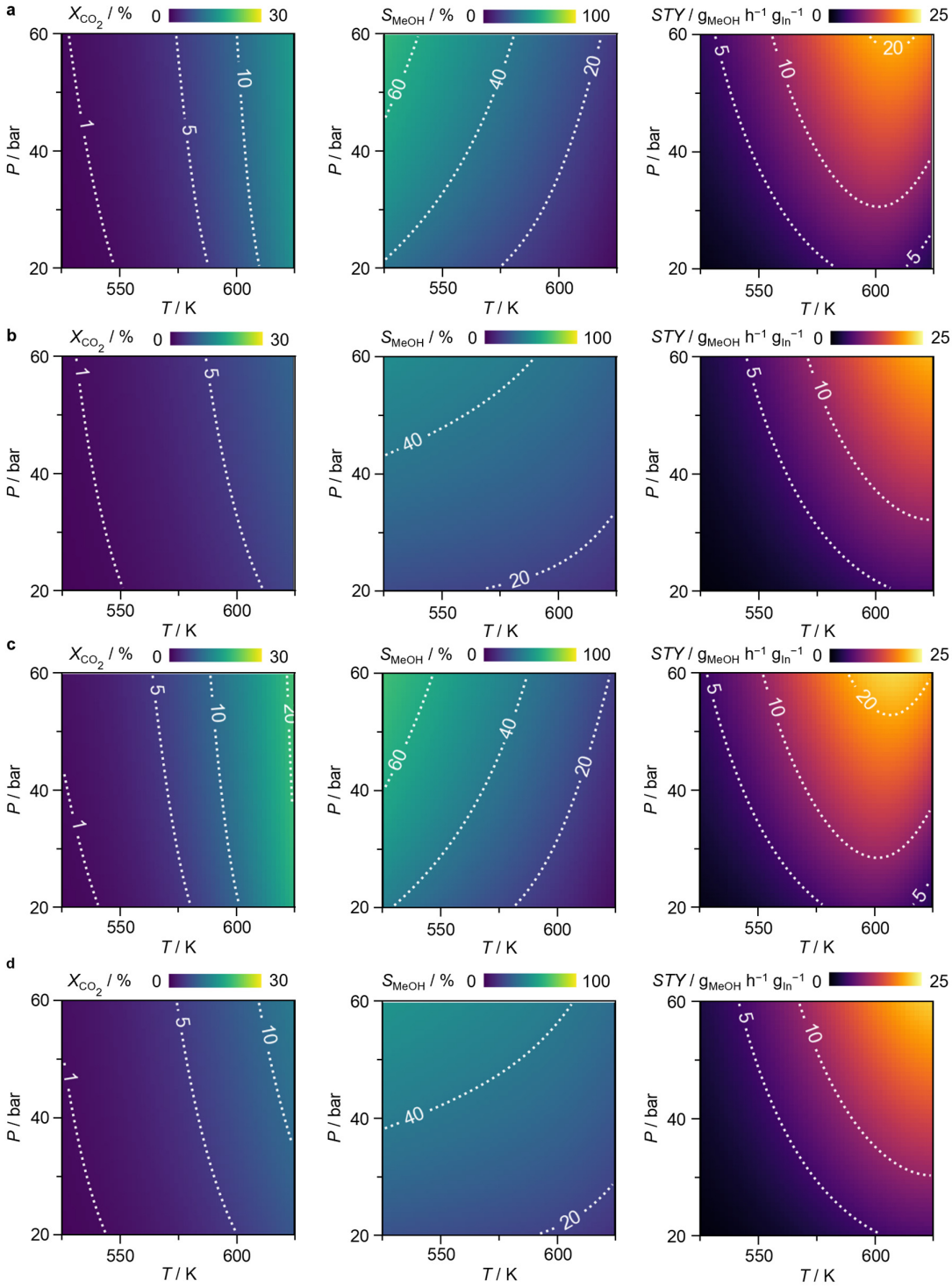

Supplementary Fig. 47. Kinetic model prediction of X_{CO2}, S_{MeOH}, and methanol *STY* during CO_2 hydrogenation over at **a**,**b** $H_2/CO_2 = 2$ and **c**,**d** $H_2/CO_2 = 3$ over $2InHfO_x$ (**a**,**c**) and $2InZrO_x$ (**b**,**d**) catalysts as a function of *P* and *T* at *GHSV* = 24,000 $cm^3\ h^{-1}\ g_{cat}^{-1}$.

References

1. Shin, H. et al. Zirconia and hafnia polymorphs: Ground-state structural properties from diffusion Monte Carlo. *Phys. Rev. Mater.* **2**, 075001 (2018).
2. Mukhopadhyay, A. B., Sanz, J. F. & Musgrave, C. B. First-principles investigation of hydroxylated monoclinic HfO_2 surfaces. *Chem. Mater.* **18**, 3397-3403 (2006).
3. Christensen, A. & Carter, E. A. First-principles study of the surfaces of zirconia. *Phys. Rev. B* **58**, 8050-8064 (1998).
4. Ricca, C., Ringuedé, A., Cassir, M., Adamo, C. & Labat, F. A comprehensive DFT investigation of bulk and low-index surfaces of ZrO_2 polymorphs. *J. Comput. Chem.* **36**, 9-21 (2015).
5. Araújo, T. P. et al. Flame-made ternary Pd-In_2O_3-ZrO_2 catalyst with enhanced oxygen vacancy generation for CO_2 hydrogenation to methanol. *Nat. Commun.* **13**, 5610 (2022).
6. Zou, T. et al. Descriptors of $InZrO_x$ vs $ZnZrO_x$ catalysts for CO_2 hydrogenation to methanol. *Adv. Energy Mater.* **15**, 2404967 (2025).
7. Araújo, T. P. et al. Design of flame-made $ZnZrO_x$ catalysts for sustainable methanol synthesis from CO_2. *Adv. Energy Mater.* **13**, 2204122 (2023).
8. Zou, T. et al. Design of technical ZnO/ZrO_2 catalysts for CO_2 hydrogenation to green methanol. *J. Catal.* **430**, 115344 (2024).
9. Jain, A. et al. Commentary: the Materials Project: A materials genome approach to accelerating materials innovation. *APL Mater.* **1**, 011002 (2013).